Available online at www.sciencedirect.com
SCIENCE DIRECT®
Journal of Sound and Vibration 292 (2006) 148–178
JOURNAL OF SOUND AND VIBRATION
www.elsevier.com/locate/jsvi

Numerical modelling of the spatial acoustic response of the human pinna

Yuvi Kahana*, Philip A. Nelson

Institute of Sound & Vibration Research, University of Southampton, Highfield SO17 1BJ, UK

Received 15 December 2004; received in revised form 10 June 2005; accepted 19 July 2005
Available online 28 October 2005

Abstract

This paper is concerned with the spatial acoustic response of the human pinna modelled with the boundary element method (BEM). Accurate geometric models of five pinnae are captured by using state-of-the-art 3-D laser scanners and digitisers. These computer models are converted to valid BEM models and analysed acoustically up to 20 kHz. Using baffled pinnae models, we first repeat and validate numerically the normal concha modes as measured in the classical experiments made by E.A.G. Shaw in the 1970s. We then study the spatial mode shapes of a baffled cylinder (as a simplified model of the concha) and accurate pinnae by applying the singular value decomposition (SVD) technique. The method is used to analyse at discrete frequencies a matrix of Green functions relating the acoustic pressure at 'field' points and 'source' points in space. We demonstrate how the singular vectors which appear as spatial mode shapes couple to the singular vectors of the sound field. The relationship between these basis functions found with the SVD and the normal concha mode shapes is demonstrated. The method is also used in producing 'reduced order' transfer functions by taking into account only the most dominant features of the singular vectors for the cases of a baffled cylinder and accurate baffled pinnae.
© 2005 Elsevier Ltd. All rights reserved.

1. Introduction

The localisation of sound sources by humans can be accomplished by the use of acoustical cues only. The head-related transfer functions (HRTFs) represent the linear, directional transformations of sound signals in free-field, detected in the eardrum of a listener or an artificial head. These functions have a complex structure, especially at frequencies above 5 kHz, with contributions being from the head, torso, and especially the external ear (outer ear). It has been shown by Kahana [1] that numerical modelling can be used to simulate the HRTFs and sound fields around the human head. The results, obtained with the boundary element method (BEM), were validated with high accuracy against measurements [2,3], and therefore it is possible to investigate further the acoustical characteristics of the human pinna with simulation tools rather than measurements.

*Corresponding author. Phone-Or Ltd., 17 Hata'asia St., Or-Yehuda 60212, Israel.
E-mail address: Yuvi@phone-or.com (Y. Kahana).

0022-460X/$ - see front matter © 2005 Elsevier Ltd. All rights reserved.
doi:10.1016/j.jsv.2005.07.048

The pinna acts as a complex acoustical antenna and codes spatial characteristics of the sound field into temporal and spectral attributes. In defining the acoustical features of the human pinna in relation to localisation cues, two schools of thought have emerged in the last 30 years. It was initially suggested by Batteau [4] that the pinna acts as a 'time domain' filter. It is more commonly recognised now that the pinna acts as a 'frequency domain' filter following the significant work presented by Shaw [5–9]. We adopt the latter approach in our study (an extensive literature survey can be found in Ref. [10]).

The largest hollow in the pinna, the concha, is a broad shallow cavity with substantial radiation damping. It is partially divided by the crus helias. The lower part, the cavum, is tightly coupled to the canal whereas the upper part, the cymba, is connected to the fossa of helix (Fig. 1, Shaw [9]). It was found [11] that these parts have acoustical attributes, whereas the structures extending from the concha, such as the helix, anti-helix and lobule seem to function collectively as a flange.

Although the response of the pinna is very complex at high frequencies and it is very sensitive to the geometric shapes, size and orientation, it is hypothesised that common physical features exist, and these appear in the form of acoustic modes, which can be used in modelling the pinna-related transfer function (PRTF) or the HRTF. Shaw [6,9] identified six different modes of the human concha. His patterns ([9, p. 38], also shown in Fig. 2) were the average among ten subjects. Although the excitation angle, the magnitude at the base of the concha and the resonance frequencies varied between individuals, his identification of monopole, 'horizontal' and 'vertical' dipole patterns provides a very important insight into understanding the physics of the external ear. These common features have not been used by Shaw in the construction of individualised response, but they were used in the construction of an average pinna. To the best of the author's knowledge his work has not been validated or continued, except for the support offered by the work of Middlebrooks [12], who observed a change in the directional response at 8 and 12 kHz, suggesting correlation with the change of pinna modes from 'vertical' dipoles to 'horizontal' dipoles.

In the last two decades, various computer simulation techniques have been suggested to model the modification of sound impinging on the human head or parts of the external ear. Weinrich [13] was the first to attempt modelling the response around an 'accurate' geometry of the head. He used analytical and numerical techniques in analysing the response of various parts of the head. He suggested a very simple geometric model

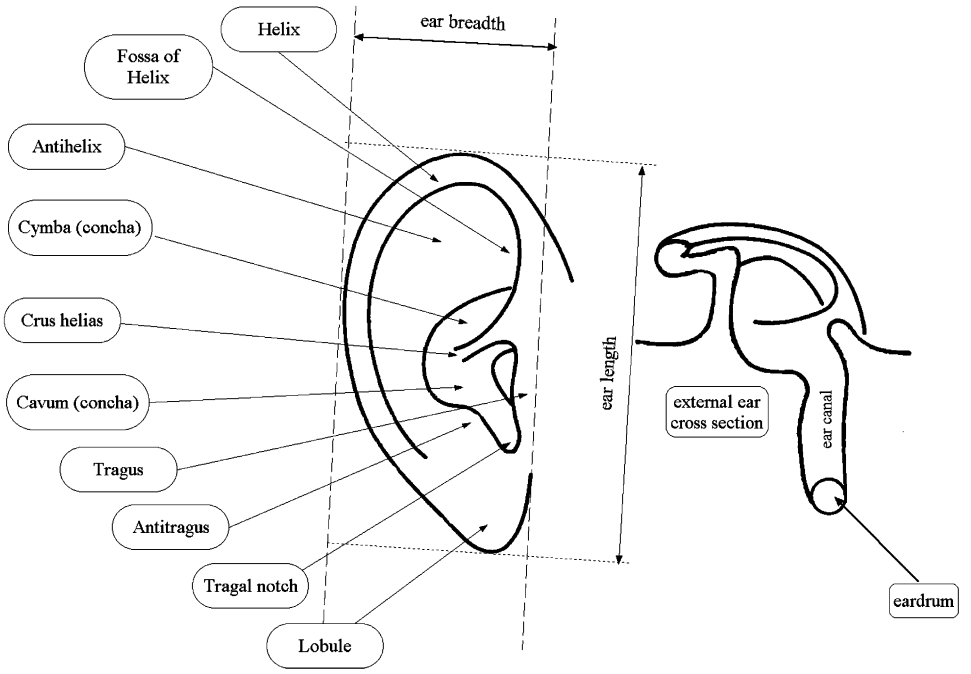

Fig. 1. The external ear. On the left, the different parts of the pinna and on the right a schematic cross section with the ear canal and eardrum. After Shaw [9].

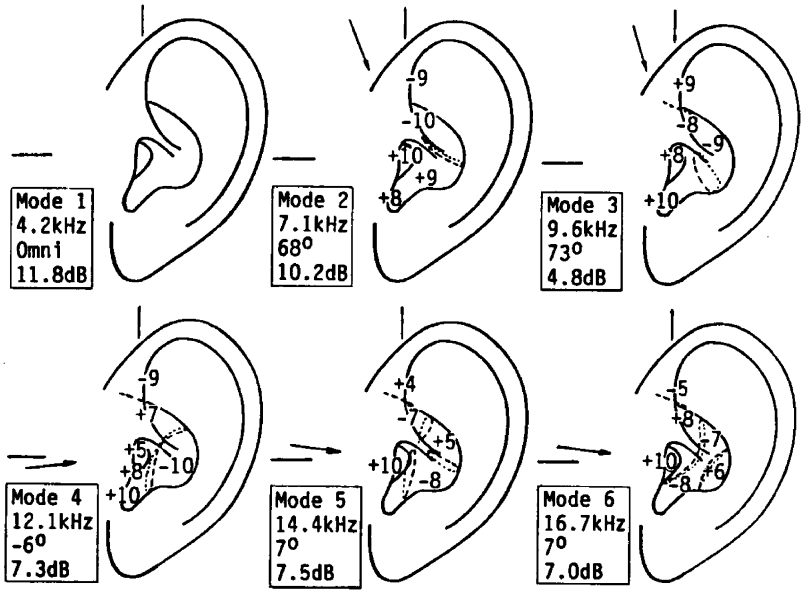

Fig. 2. Average characteristics of six modes under blocked meatus conditions based on data for ten subjects. Numbers indicate relative values of sound pressure, on a linear scale, measured at base of the concha. Signs (±) indicate relative phase (0°/180°). Broken and dotted lines show positions of nodal surfaces. Arrow indicates most favourable source direction. Data at left show mode number, mode frequency, most favourable source angle, and mode response. Mode 1 has uniform pressure across base of concha and is approximately omnidirectional. (After Shaw [7,9]).

of the pinna with a mesh of only 20 elements resembling the shape of the concha. His solution was based on a finite difference approximation method, and the results approximated only roughly the dependence of the first notch with elevation. Recently, Katz [14,15] acquired individualised HRTFs using the BEM. Although the idea was similar to the work of Weinrich, the use of BEM models converted from accurate laser-scanned models suggested that although the BEM is associated with 'low-frequency' modelling, we can now solve tens of thousands of simultaneous equations, in order to predict the response of complex shapes such as the human head. Owing to limited computing power, his work was restricted to frequencies below 5 kHz; as a result, his simulations could not be validated in the high-frequency range where pinna resonance and anti-resonance affect the pressure variations.

In this paper, we focus on accurate acoustic modelling of the external ear with the emphasis on acoustic modes (the PRTFs and HRTFs are discussed in Refs. [2,3]), where first we attempt to repeat Shaw's experiment by computer simulation, and later we derive a mathematical formulation that can extract the modal characteristics of an individual pinna into its frequency response. The foundations of the formulation used in this paper were presented in Refs. [16,17]). In these papers, the authors investigated the relationship between the basis functions of classical acoustics and the singular value decomposition (SVD) through the scattering from a rigid sphere where the response of a sphere was derived using an infinite series of complex spherical harmonics. This formulation was used in the construction of a Green function matrix relating a number of field points in the far field (on a large sphere) and a number of sources on the surface (of a small sphere). In Ref1. [17], the authors described the relationship between the 'mode shapes' and the spherical harmonics, and discussed the effect of non-uniform sampling of either the radiating surface or the far field. This influences the interpretation of the SVD when using arbitrary, complex, radiating or scattering shapes such as human pinnae that are investigated in this paper.

We hypothesise that at a specific 'resonance' frequency, the dominant singular value σ_1 will have significantly higher amplitude than the others, and the complex singular vectors associated with this singular value will have distinctive patterns. We compare these patterns, and their resonance frequencies with the

results of Shaw's study of the normal modes. We also show how the baffled pinna frequency response can be reconstructed using only a few of the dominant singular values.

2. Boundary element method and mesh models

2.1. BEM formulation

2.1.1. Direct boundary integral equation

The numerical simulations below were undertaken using the SYSNOISE software package [18] which uses the BEM in order to compute numerically the solution of the homogeneous Helmholtz equation. This Direct BEM is given by

$$p(\mathbf{r}) = \int_s [p(\mathbf{r}_0)\frac{\partial g(\mathbf{r}|\mathbf{r}_0)}{\partial n} - g(\mathbf{r}|\mathbf{r}_0)\frac{\partial p(\mathbf{r}_0)}{\partial n}]\,\mathrm{d}S(\mathbf{r}_0), \tag{1}$$

which is Kirchhoff–Helmholtz integral equation. SYSNOISE first solves the integral equation for the surface pressure $p(\mathbf{r}_0)$. More details are given in Refs. [18,19].

2.1.2. Indirect boundary integral equation

The DBEM can be used only when the boundary surface S is closed, thus the sound field can be calculated either inside *or* outside the boundary surface. For cases where the domain is open, or includes both closed *and* open boundary surfaces, the indirect boundary element method (IBEM) is used (see Ref. [20]).

$$p(\mathbf{r}) = \int_s \left[\mu(\mathbf{r}_0)\frac{\partial g(\mathbf{r}|\mathbf{r}_0)}{\partial n} - \sigma(\mathbf{r}_0)g(\mathbf{r}|\mathbf{r}_0)\right]\mathrm{d}S(\mathbf{r}_0) \quad (\mathbf{r} \in V), \tag{2}$$

where $\mu(\mathbf{r}_0) = p^+(\mathbf{r}_0) - p^-(\mathbf{r}_0)$ is generally called the jump of pressure or the *double layer potential.* It represents a distribution of *dipole* sources on the surface, and $\sigma(\mathbf{r}_0) = ((\partial p^+(\mathbf{r}_0))/\partial n) - ((\partial p^-(\mathbf{r}_0))/\partial n)$ is generally called the jump of normal derivative of pressure or *single layer potential*, and it represents a distribution of *monopole* sources on the surface. The term $g(\mathbf{r}|\mathbf{r}_0)$ represents the free space Green function relating the pressure at $\mathbf{r}$ to the source strength at $\mathbf{r}_0$.

2.1.3. Acoustic transparency in the IBEM

The following formulation of the IBEM is a special case of the integral equation. Its main use is in problems where the transmissibility of sound by vibro-acoustic interactions can be analysed on both sides of an infinite baffle.

The pressure can be analysed as a superposition of the contribution by the single and double layer potentials on the three parts of S: S^l, the part of S in V^-, S^m, the part of S in the infinite plane, and S^r, the part of S in V^+ (see Fig. 3).

It is shown in detail by Coyette et al. [21], that the total pressure is given by

$$\begin{aligned} p(\mathbf{r}) = &\int_{S^m}\left\{+\frac{\partial p^-(\mathbf{r}_0)}{\partial n}g(\mathbf{r}|\mathbf{r}_0)\right\}\mathrm{d}S(\mathbf{r}_0) + \int_{S^l}\left\{\mu(\mathbf{r}_0)\frac{\partial g(\mathbf{r}|\mathbf{r}_0)}{\partial n} - \sigma(\mathbf{r}_0)g(\mathbf{r}|\mathbf{r}_0)\right\}\mathrm{d}S(\mathbf{r}_0) \\ &+ \int_T\left\{-\frac{\partial p(\mathbf{r}_0)}{\partial n}g(\mathbf{r}|\mathbf{r}_0)\right\}\mathrm{d}S(\mathbf{r}_0) \quad (\mathbf{r} \in V^-) \end{aligned} \tag{3}$$

and

$$\begin{aligned} p(\mathbf{r}) = &\int_{S^m}\left\{-\frac{\partial p^+(\mathbf{r}_0)}{\partial n}g(\mathbf{r}|\mathbf{r}_0)\right\}\mathrm{d}S(\mathbf{r}_0) + \int_{S^r}\left\{\mu(\mathbf{r}_0)\frac{\partial g(\mathbf{r}|\mathbf{r}_0)}{\partial n} - \sigma(\mathbf{r}_0)g(\mathbf{r}|\mathbf{r}_0)\right\}\mathrm{d}S(\mathbf{r}_0) \\ &+ \int_T\left\{-\frac{\partial p(\mathbf{r}_0)}{\partial n}g(\mathbf{r}|\mathbf{r}_0)\right\}\mathrm{d}S(\mathbf{r}_0) \quad (\mathbf{r} \in V^+), \end{aligned} \tag{4}$$

where the integrals over T refer to the elements depicted in Fig. 3.

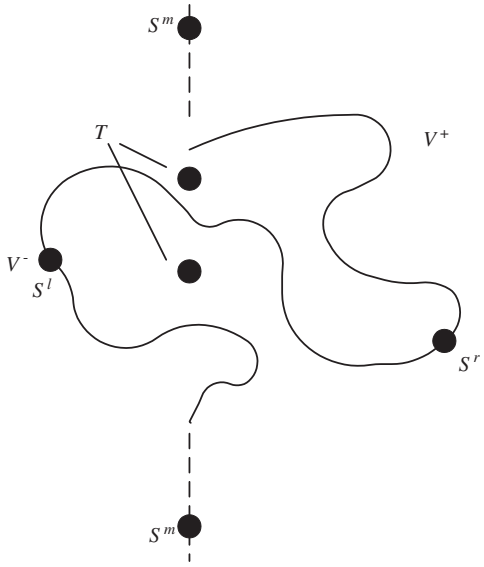

Fig. 3. Acoustic transparency: a sound wave can propagate from both sides of the baffle (V^- and V^+) through 'transparent' elements (at points T) defined at $z = 0$. S^m denotes the points on the infinite baffle, and S^r and S^l the points on surface of the body attached to the baffle, on the positive and negative sides of the baffle, respectively.

2.2. Acquiring the computer models

The initial assumption made during this work was that the highest resolution possible is required for the mesh models of the pinnae. There are currently a few techniques available to obtain a computer model by scanning a physical model. These include computed tomography (CT), magnetic resonance imaging (MRI), 3-D ultrasonic imaging, etc. These are generally used for internal scanning for medical purposes. The main advantage of the 3-D laser scanner technique used in this research is that it can produce fairly quickly an accurate mesh of the surface made out of triangles.[1] The Cyberware 'Mini model' 3-D laser scanner is based on the high-resolution 3030RGB/HIREZ scan head with a mid-size high-resolution motion system. With this scanner, even the ear canal geometry can be obtained.

2.3. Mesh decimation

The original scan produced a polygonal mesh (see Ref. [22] for details) that describes the surface geometry of the pinna. Since the CPU time of the BEM increases drastically with the number of nodes, it is crucial to optimise the size of the mesh. It is well known that the maximum frequency in the BEM corresponds to the longest edge in the mesh. Any alteration to this global limit will distort the overall results. Therefore, a homogeneous distribution of the nodes and elements is required.

The main algorithm used in this research has been developed by Johnson and Hebert [23] where its main advantage is in successfully handling the two forces in mesh decimation: preserving the shape by limiting a defined maximum 'global shape error' and distributing the vertices homogeneously by local operators. This algorithm and more mesh manipulation techniques required in this study are described in detail in Ref. [1].

2.4. Pinnae mesh models

A few pinnae were scanned and investigated. Four pinnae of KEMAR [24] (the right pinnae: DB-60, DB-65, DB-90 and DB-95), B&K [25], CORTEX [26,27], and YK (the first author's moulded model). Since DB-95

[1]Note that in principle, the use of quadrilateral elements can produce a higher accuracy of the simulation compared with triangular elements, but due to the format of the original data, quarilateral elements were not used for scanned models.

does not represent a typical human ear, it was found that the resulting response was not representative of a typical ear, and it was decided not to include it in the following analysis of the results. Also, the DB-90[2] was used only in the study of normal concha modes.

The original models included approximately 150,000 triangles and 75,000 vertices, and included three-dimensional information of the pinna (including its frame and base). The final BEM mesh models used in this study were composed of, on average, 7400 triangles and 3800 vertices (also termed 'elements' and 'nodes', respectively, in the context of BEM).

3. Normal mode extraction of baffled pinna models

3.1. The original experimental apparatus and procedure

In this section, we extract with numerical modelling the normal modes of the pinna, following a similar experimental procedure as was used by Shaw [6,7] using the coordinate system which is illustrated in Fig. 4. Shaw attached a plate to the head, so that diffraction around the head was minimised. A progressive wave source was rotated in the grazing incidence plane ($0^\circ \leqslant \theta < 360^\circ, \phi = 0^\circ$) and the pressure was measured with a probe microphone at the blocked meatus position. The variation of pressure under these conditions resembles the response under free-field conditions for median plane sources. A mode was found when maxima appeared as the frequency and source positions were moved. Then the pressure amplitude and phase were recorded at the base of the concha and the fossa of helix as well as the angle at which the mode was most excited.

3.2. Numerical modelling

In order to model an infinite baffle, all pinnae boundaries are aligned to a specific plane ($z = 0$). The mesh models that were used had a maximum distance of 3.7 mm (on average) from one vertex (node) to another which corresponded to a maximum frequency of ~15 kHz assuming six elements per wavelength and ~23 kHz when assuming four elements per wavelength. Two types of models were investigated. The first, shown in Fig. 5(a), is characterised with gradual smooth alignment of the boundaries of the pinna to the baffle plane. The algorithms used to manipulate the model did not change any of the geometrical dimensions of the pinna itself. This model also includes a refined area around the blocked meatus position for using the principle of reciprocity (see below). The second model, shown in Fig. 5(b), is optimised to give the minimal number of elements and nodes due to the complexity of the calculation used in Section 5.

In the numerical modelling of this experiment, the small baffle Shaw attached to his subjects around their pinnae is replaced here by an infinite baffle. His 'wave progressive source' is replaced here first[3] by an ideal monopole source that is placed 1 mm away from the blocked meatus. Using the principle of reciprocity, this is used to calculate the pressure variations 1 m away (Shaw was limited to the near field only with a distance of 8 cm from the microphone, due to the size of the baffle and calibration of the transducers). With the reciprocity simulation technique, the calculation of the pressure at field points in the post-process stage is straightforward and fast. However, we limited these points to be on a circle with a radius of 1 m at grazing incidence. The calculation is undertaken at a resolution of 1°, and the frequency step was 200 Hz from 1 to 20 kHz. It is assumed that if the pressure at the blocked meatus position is predicted accurately, other points on the surface of the pinna should have a similar accuracy. These are obtained immediately due to the inter-connectivity of the BEM equation where *all* pressure values on the surface are solved for simultaneously.

It should be noted that a common problem associated with exterior problems solved with the DBEM is that the solution breaks down at certain characteristic frequencies. As demonstrated by Schenck [28], these frequencies are the eigenfrequencies of the corresponding interior problem with modified boundary conditions. These frequencies appear purely for mathematical and not physical reasons. In total, 30 over-determination points were used in our modelling cases to alleviate this problem.

[2]Note that DB-90 and DB-95 have larger ear canal openings. Their geometry is mainly suited for the use of earmoulds.

[3]This to find the maxima of pressure variation in the far field. Later a plane wave source was used to excite the pinna, to eliminate spherical attenuation.

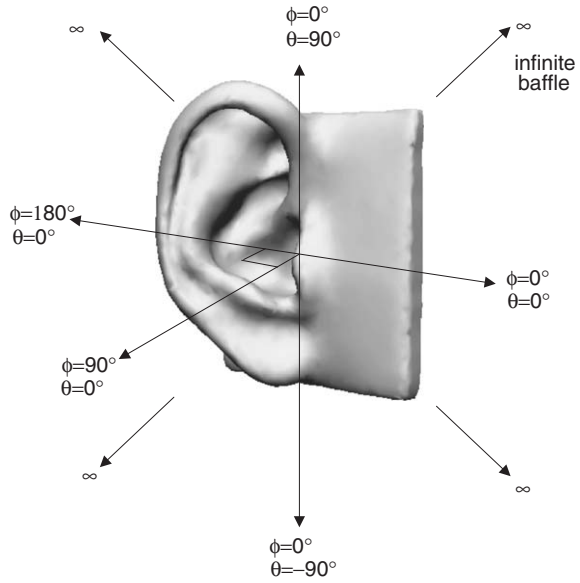

Fig. 4. Coordinate system for the simulation of the transfer function and modes of baffled pinnae.

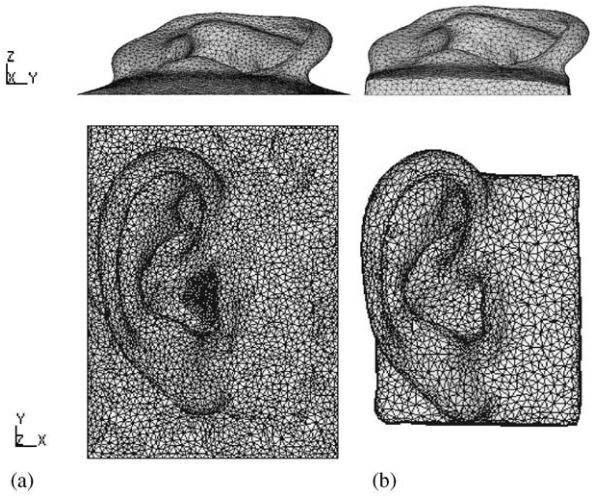

Fig. 5. (a) DB-65 BEM mesh with 5199 nodes and 10216 elements. The boundaries are smoothed gradually to the baffle plane $z = 0$. Note the mesh refinement at the base of the concha which is used when the reciprocity method is used and a source is positioned at the entrance to the blocked meatus. This model is optimised for normal modes simulation in baffled conditions. (b) Original shape with frame boundaries aligned with baffle plane, $z = 0$. Optimised for minimal size for SVD calculations (3389 nodes with 6656 elements).

3.3. Results

Fig. 6 presents the linear amplitude variations of peaks and notches as detected at the blocked meatus of DB-65 (this is a larger pinna than the original DB-60 of KEMAR, suggested by Maxwell and Burkhard, [29]) using the mesh model shown in Fig. 5(a). The amplitude colour bar values range from 0 to 4.7 times the source strength of a monopole source at 1 m. The map shows the frequency in the x-axis and the angle of excitation at grazing angles in the y-axis. The calculation is undertaken using the reciprocity technique where a monopole source was positioned 1 mm away from the blocked meatus location.

It can be observed that six resonance frequencies appear as follows: at 4.2, 7.2, 9.5, 11.6, 14.8, and at 18.0 kHz. The exact angle, at which the excitation is at maximum, was found by plotting a directivity/vector

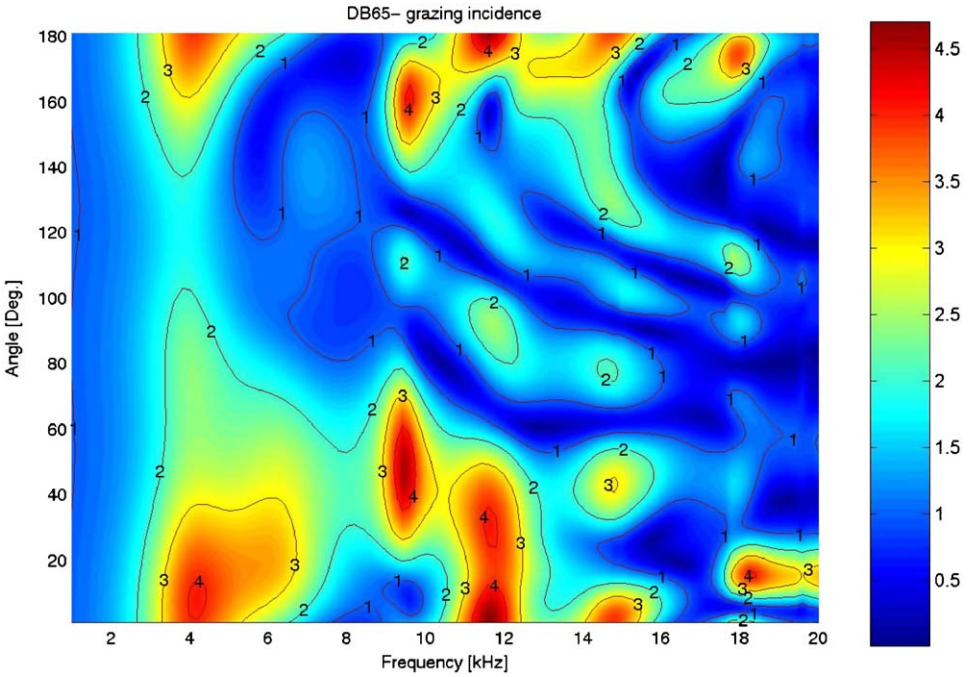

Fig. 6. The normalised response of DB-65 baffled pinnae in grazing incidence at a resolution of 1° and steps of 200 Hz. The linear values for each angle of source were obtained by dividing the response at the entrance to the blocked ear canal with the response at the same location on the baffle but without the pinna. Value of "1" means that the pinna does not contribute to pressure variations, whereas values below and higher than "1" mean attenuation and amplification, respectively.

plot, at each resonance frequency. In the left plots in Fig. 7, the length of the arrows facing the centre of the pinna corresponds to the magnitude of the pressure at the blocked meatus due to a source at that location. Also the colour of the arrow changes with the magnitude: red for maximum response and blue for minimum response. The colours assigned to each vertex on the pinna mesh (the right-hand pictures) correspond to the absolute pressure, and negative values indicate negative phase at the particular vertex (compared to the phase at the blocked entrance to the ear canal). Note that a more accurate way of presenting these results would be with two plots; either of the real and imaginary values of the pressure, or the magnitude and phase, but we use this format for consistency with Shaw's plots.

The first resonance appears in Fig. 7(a) at 4.2 kHz. The directivity plot is almost omnidirectional, i.e. the pinna is excited almost with the same efficiency from every direction in grazing incidence. The pressure variation at the base of the concha is also almost uniform with amplification factor of 4.5 compared with the response detected at the centre of the baffle (which doubles the pressure, compared to free-field equalisation).

The next two 'vertical' modes, in Fig. 7(b) and in Fig. 7(c) are excited the most effectively from the angles of $\theta = 60^\circ$ and 94°, respectively, and these are within the range measured by Shaw. Also note the nodal line appears in the vicinity of the crus helias.

The next three modes (Figs. 7(d)–(f)) are clearly 'horizontal' with all excitation having maxima at the front ($\theta = 0^\circ, 4^\circ, -16^\circ$, respectively). Also in this case, the angle variations are in agreement with Shaw's results. Also the nodal lines and phase changes have similar patterns to his measurements.

This procedure was repeated for five additional pinnae, and the resonance frequencies are summarised in Table 1. Note that not all six modes are identified with each pinna. This will be discussed in Section 6.

4. Spatial basis functions and the singular value decomposition

The SVD method is a commonly used mathematical tool in the analysis of sound radiation and scattering (for example, where the SVD is used in the context of 'mode shapes', see Refs. [30–33]). In the following

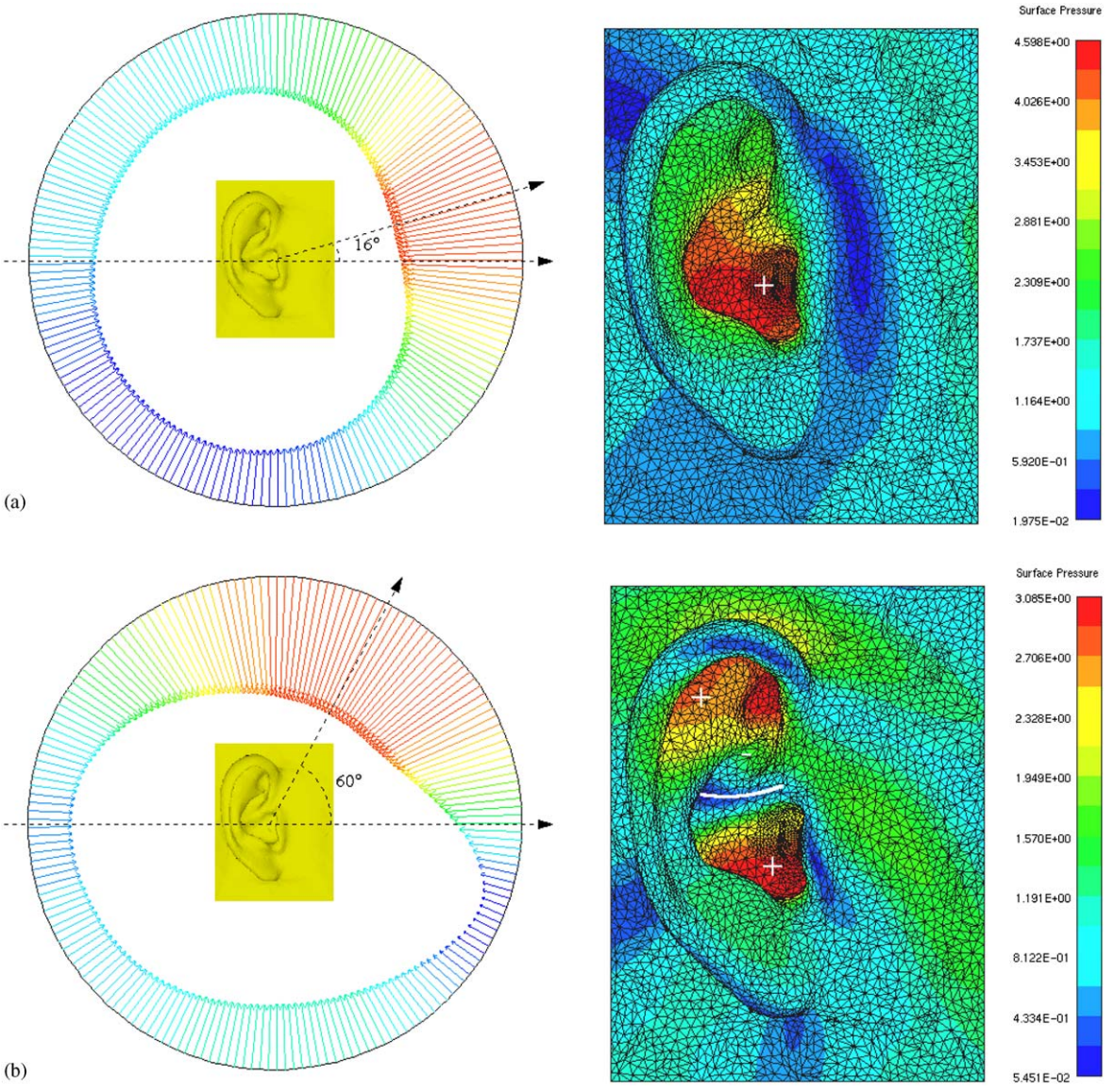

Fig. 7. The modes of the DB-65 modes with a similar format presented in Fig. 2. The figures correspond to the following frequencies: (a) 4.2 kHz, (b) 7.2 kHz, (c) 9.5 kHz, (d) 11.6 kHz, (e) 14.8 kHz, (f) 18 kHz.

section, we concentrate on the problem of sound radiation (or scattering) from arbitrary, complex shapes. A detailed description of the theory below is given in Ref. [1] and in Refs. [13,17].

4.1. The singular value decomposition (SVD) method

A matrix $\mathbf{G}(\mathbf{r}|\hat{\mathbf{r}})$ of Green functions is defined by relating the pressure $\mathbf{p}$ produced at a number of field points specified by the positions $\mathbf{r}$ to a number of point (monopole) sources specified at positions $\hat{\mathbf{r}}$ with source strengths $\mathbf{q}$. Thus the pressure can be expressed as

$$\mathbf{p}(\mathbf{r}) = \mathbf{G}(\mathbf{r}|\hat{\mathbf{r}})\mathbf{q}(\hat{\mathbf{r}}). \tag{5}$$

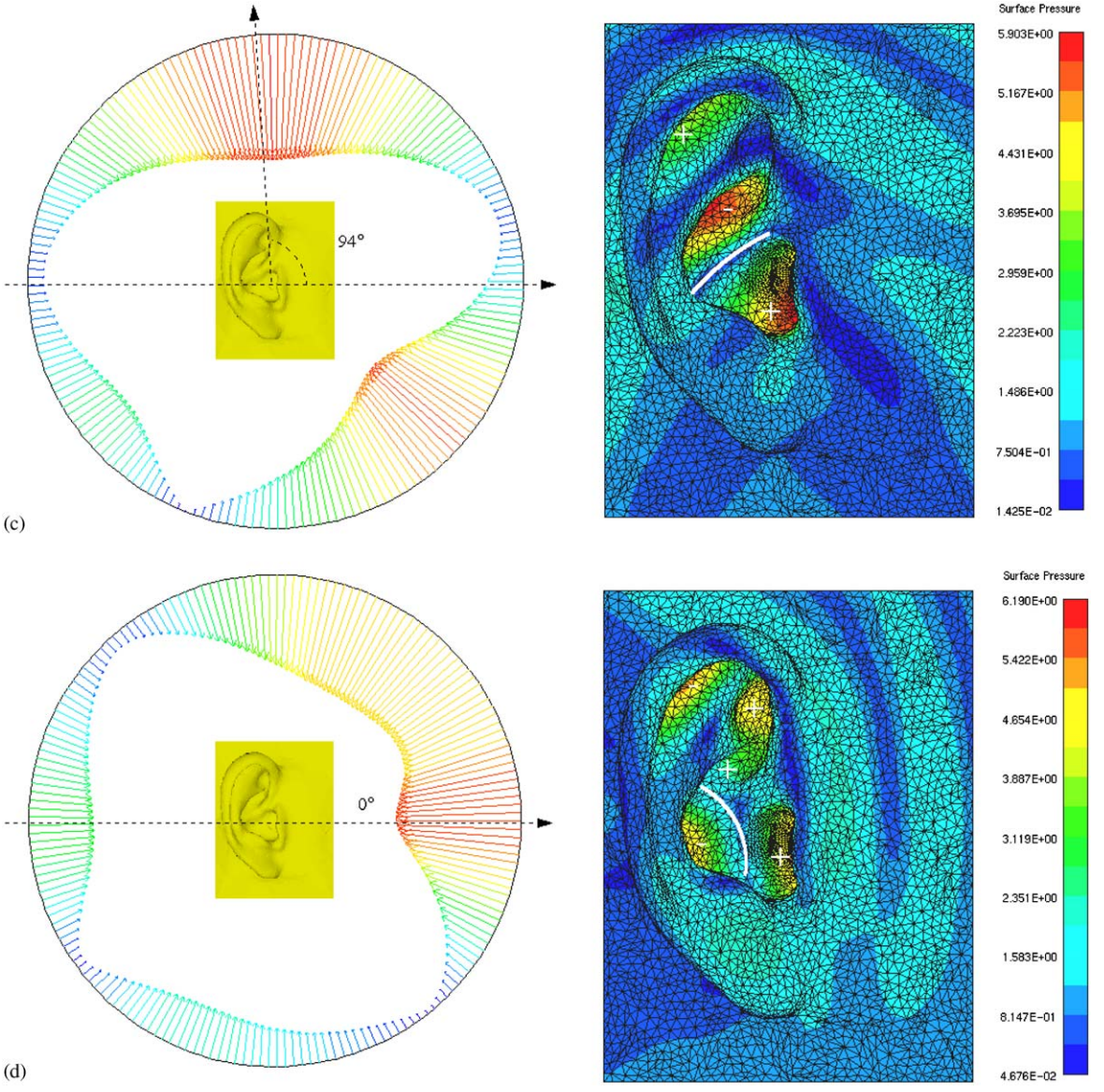

Fig. 7. (*Continued*)

The SVD method enables any complex matrix with dimensions $K \times L$ to be expressed as

$$\mathbf{G}(\mathbf{r}|\hat{\mathbf{r}}) = \mathbf{U} \sum \mathbf{V}^{\mathrm{H}}, \tag{6}$$

where $\sum$ is the $K \times L$ matrix whose elements are zero except the diagonal elements σ_i. The superscript H denotes conjugate transpose. Note that the singular values are always arranged in a descending order and the rank R of $\mathbf{G}(\mathbf{r}|\hat{\mathbf{r}})$ can be smaller than the size of K or L such that

$$\sigma_1 \geqslant \sigma_2 \geqslant \cdots \sigma_R > 0, \sigma_{R+1} = \cdots = \sigma_p = 0 \quad p = \min(K, L). \tag{7}$$

The matrices $\mathbf{U}$ and $\mathbf{V}$ are square matrices with the dimension $K \times K$ and $L \times L$, respectively, and are orthogonal such that

$$\mathbf{U}^{\mathrm{H}}\mathbf{U} = \mathbf{U}\mathbf{U}^{\mathrm{H}} = \mathbf{I}, \quad \mathbf{V}^{\mathrm{H}}\mathbf{V} = \mathbf{V}\mathbf{V}^{\mathrm{H}} = \mathbf{I}. \tag{8}$$

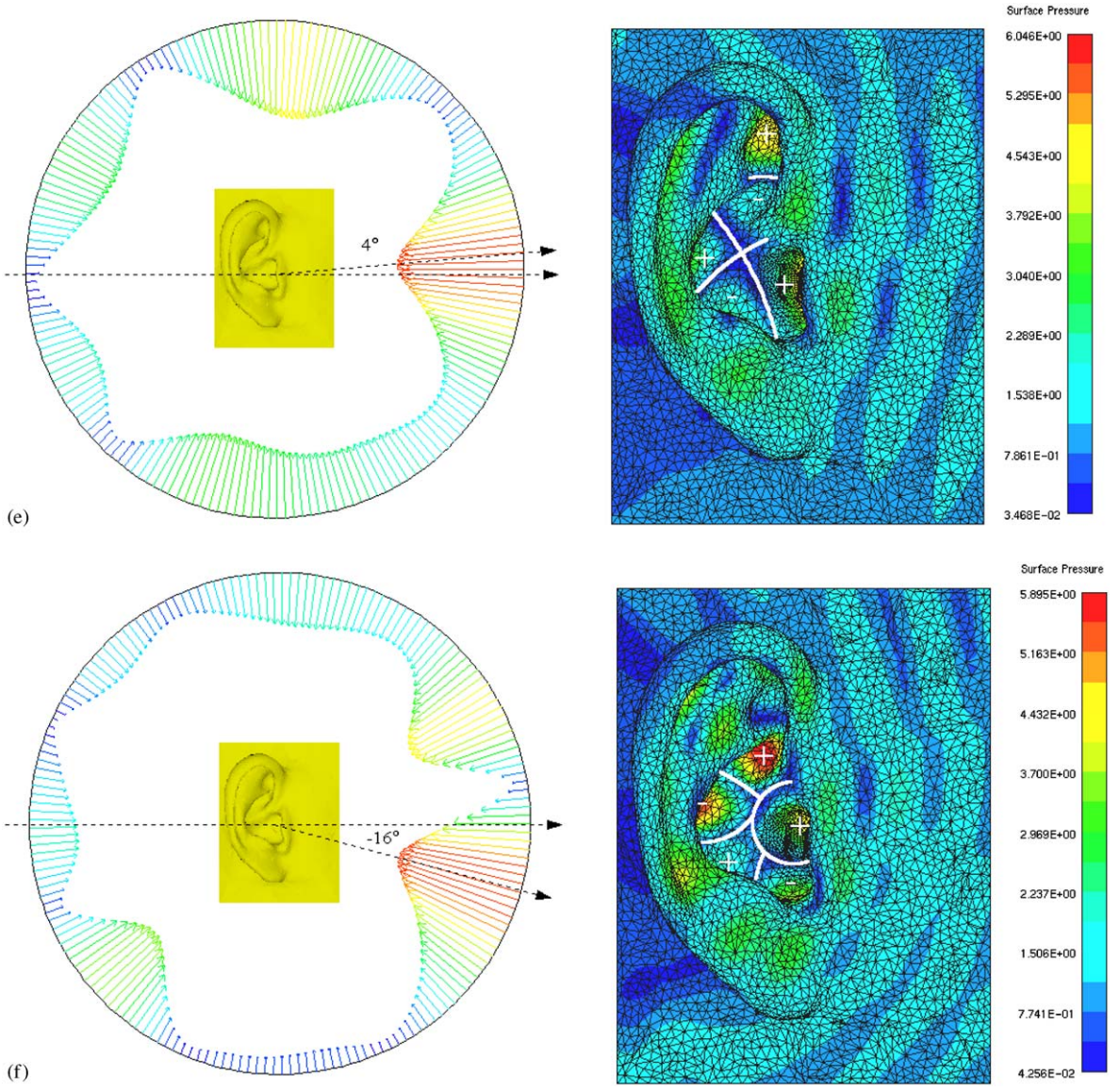

Fig. 7. (*Continued*)

The columns $\mathbf{u}_i$ of the matrix $\mathbf{U}$ and the columns $\mathbf{v}_i$ of the matrix $\mathbf{V}$, respectively, define the left and right singular vectors of $\mathbf{G}(\mathbf{r}|\hat{\mathbf{r}})$. These singular vectors can be interpreted as 'mode shapes' since they provide sets of orthogonal basis functions for describing the spatial variation in radiated pressure and their relationship to spatial variations in source strength. Specifically, it follows from Eqs. (1) and (2) that

$$\mathbf{p}(\mathbf{r}) = \mathbf{U} \sum \mathbf{V}^{\mathrm{H}} \mathbf{q}(\hat{\mathbf{r}}) \tag{9}$$

and since $\mathbf{U}^{-1} = \mathbf{U}^{\mathrm{H}}$, this expression can be rearranged as

$$\mathbf{U}^{\mathrm{H}} \mathbf{p}(\mathbf{r}) = \sum \mathbf{V}^{\mathrm{H}} \mathbf{q}(\hat{\mathbf{r}}). \tag{10}$$

It follows that we may write for all $i \leqslant P, (P = \min(K, L))$

$$\mathbf{u}_i^{\mathrm{H}} \mathbf{p}(\mathbf{r}) = \sigma_i \mathbf{v}_i^{\mathrm{H}} \mathbf{q}(\hat{\mathbf{r}}). \tag{11}$$

Table 1
Resonance frequencies in kHz of six pinnae modelled with the BEM. The frequency corresponds to the frequency at which the maximum amplification is reached in the resonance frequency range. The results of Shaw [9] show the average of 10 pinnae

DB-60	DB-65	DB-90	YK	CORTEX	B&K	Shaw
4.9	4.2	4.2	4.1	4.2	4.1	4.2
7.8	7.2	7.2	7.6	7.2	7.7	7.1
10.3	9.5	9.6	—	9.6	10.5	9.6
—	11.6	11.8	11.2	11.8	12.2	12.2
14.0	14.8	14.7	14.0	14.1	15.3	14.4
17.0	18	18.4	17.8	17.4	18.0	16.7

This expression demonstrates that at a certain frequency a spatial pattern in the radiated field defined by $\mathbf{u}_i^{\mathrm{H}}\mathbf{p}(\mathbf{r})$ is linearly related to a specific spatial pattern of source strength distribution defined by $\mathbf{v}_i^{\mathrm{H}}\mathbf{q}(\hat{\mathbf{r}})$. These two patterns are related by the singular value σ_i.

Note that it is possible using the SVD formulation to reconstruct the frequency response from a source in a particular position p_n and a field point in another position q_m. Based on Eq. (6), the vector $\mathbf{p}$ can be given by the product

$$\begin{bmatrix} p_1 \\ p_2 \\ \vdots \\ p_n \\ \vdots \\ p_N \end{bmatrix} = \begin{bmatrix} u_{11} & u_{21} & \cdots & u_{n1} & \cdots & u_{N1} \\ u_{12} & u_{22} & \cdots & u_{n2} & \cdots & u_{N2} \\ \vdots & \vdots & \ddots & \vdots & \vdots & \vdots \\ u_{1n} & u_{2n} & \cdots & u_{nn} & \cdots & u_{Nn} \\ \vdots & \vdots & \vdots & & \ddots & \vdots \\ u_{1N} & u_{2n} & \cdots & u_{nN} & \cdots & u_{NN} \end{bmatrix} \begin{bmatrix} \sigma_1 & & & & & \\ & \sigma_2 & & & & \\ & & \ddots & & & \\ & & & \sigma_n & & \\ & & & & \ddots & \\ & & & & & \sigma_N \end{bmatrix} \times \begin{bmatrix} v_{11}^* & v_{12}^* & \cdots & v_{1n}^* & \cdots & v_{1N}^* \\ v_{21}^* & v_{22}^* & \cdots & v_{2n}^* & \cdots & v_{2N}^* \\ \vdots & \vdots & \ddots & \vdots & \vdots & \vdots \\ v_{m1}^* & v_{m2}^* & \cdots & v_{mn}^* & \cdots & v_{mN}^* \\ \vdots & \vdots & \vdots & \vdots & \vdots & \vdots \\ v_{M1}^* & v_{M2}^* & \cdots & v_{Mn}^* & \cdots & v_{MN}^* \end{bmatrix} \begin{bmatrix} q_1 \\ q_2 \\ \vdots \\ q_m \\ \vdots \\ q_M \end{bmatrix}. \tag{12}$$

For the case of an excitation due to a specific source, we assume only q_m is non-zero, then

$$\begin{bmatrix} p_1 \\ p_2 \\ \vdots \\ p_n \\ \vdots \\ p_N \end{bmatrix} = \begin{bmatrix} u_{11} & u_{21} & \cdots & u_{n1} & \cdots & u_{N1} \\ u_{12} & u_{22} & \cdots & u_{n2} & \cdots & u_{N2} \\ \vdots & \vdots & \ddots & \vdots & \vdots & \vdots \\ u_{1n} & u_{2n} & \cdots & u_{nn} & \cdots & u_{Nn} \\ \vdots & \vdots & \vdots & & \ddots & \vdots \\ u_{1N} & u_{2n} & \cdots & u_{nN} & \cdots & u_{NN} \end{bmatrix} \begin{bmatrix} \sigma_1 v_{1m}^* q_m \\ \sigma_2 v_{2m}^* q_m \\ \vdots \\ \sigma_n v_{nm}^* q_m \\ \vdots \\ \sigma_N v_{Nm}^* q_m \end{bmatrix} \tag{13}$$

or in a compact form

$$p_n = \sum_{n=1}^{N} \sigma_n u_{nn} v_{nm}^* q_m. \tag{14}$$

Thus, the summation can be limited to a number which is less than N, if the last terms of the series of σ_n are much smaller than the first terms.

5. Spatial basis functions of baffled pinna models using the singular value decomposition

5.1. The cylinder in an infinite baffle

5.1.1. The singular values

The cylinder, as a basic model of the concha was investigated by Shaw and Teranishi [5] in their early work. Since the first resonance of a blocked meatus pinna corresponds to a quarter wavelength 'depth' mode, it is possible to match the volume of a cylinder to produce the desired resonance frequency as well as controlling the amplification at its base. In this case, we use a cylinder model where its entire top section is defined as transparent (see Fig. 8(a)). A model with similar dimensions was investigated by Teranishi and Shaw [11] who showed that the first resonance frequency around 4.5 kHz is determined by the volume of the cylinder. The response is substantially independent of the angle of incidence up to about 7 kHz but becomes strongly dependent on the angle of excitation at the first transverse mode at approximately 11 kHz (see Teranishi and Shaw, Fig. 2(b), [11]). As before, the calculation was undertaken using the 'IBEM transparency' formulation.

Clearly, the characteristics of the singular values depend on the geometry of the radiating body as well as the source positions defined in the Green function matrix. By defining the field points not only at the bottom of the cylinder but also on the cylinder walls and on a small area on the baffle, the properties of the singular values can be investigated where some parts of the 'radiating' body have different resonance frequencies. Therefore, the field point mesh (see Fig. 8(b)) was used to calculate the pressure values and includes 336 nodes and 457 elements. The sources were positioned for each run at one of the 121 positions defined on the upper hemisphere, composed of 108 elements.[4]

Fig. 9 presents the variation of the singular values with frequency. It can be noticed that two 'resonance' frequencies (the frequencies at which the curves of the singular values reach a peak) are characterised by strong peaks. These do not need to coincide with resonance frequencies of a particular transfer function (for example: at the base of the baffled cylinder due a source at an arbitrary location), but they have similar characteristics since these main peaks have distinctive frequencies and amplitudes (see an example in Section 5.1.3).

The first mode, at 4.2 kHz is known to be associated with a quarter wavelength depth resonance, with a peak in σ_1 only. The second mode appearing at 10.8 kHz is a transverse mode, with peaks in both σ_1 and σ_2. It is interesting to observe the connectivity and intersection between the curves, as the SVD automatically positions σ_1 before σ_2 (see Fig. 9, and Eq. (7)). It was found that when a sampled mesh of source points having an insufficient resolution was used, the same resonance frequency appeared, but the curves were not intersecting each other, as we shall see in the case of modelling of accurate representation of pinnae (Section 5.2). Following the curve of σ_1 (a 'monopole' mode), its radiation efficiency is predominant up to 4.2 kHz, and gradually decreasing with increasing frequencies. The curves of σ_2 and σ_3 ('dipole' modes) start with a similar singular value at 2 kHz and increase with frequency up to 10.8 kHz, and then have decreasing amplitude. As frequency increases, the contribution of lower-order singular values is increasing, such that at 12 kHz σ_{10} is almost 50% of σ_1. Another important conclusion that arises from this graph is that certain modes can be associated with more than a single singular value σ.

[4]It is estimated that much lower density meshes could have been sufficient, and the high resolution was used to investigate the effect on the intersection of the curves of the singular values as a function of frequency.

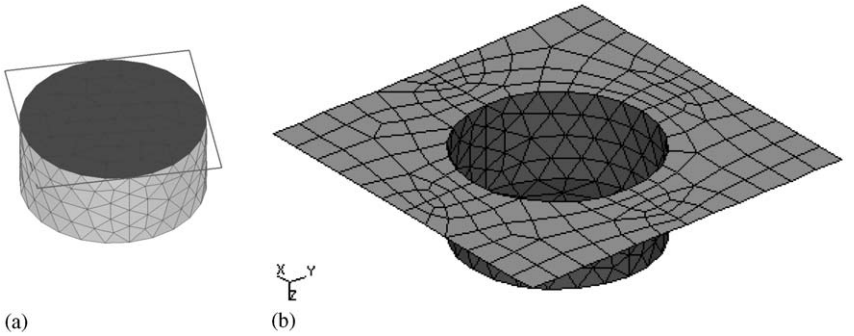

Fig. 8. The IBEM transparency mesh model: (a) A mesh cylinder with a volume of 3.8 cm^3 to represent the concha is composed of 376 linear elements and 190 nodes. Its top is aligned with the infinite baffle ($z = 0$), where all top elements are transparent so waves can propagate through both sides of the baffle. (b) 457 elements and 336 nodes of field points are located both on the walls of the cylinder and the baffle.

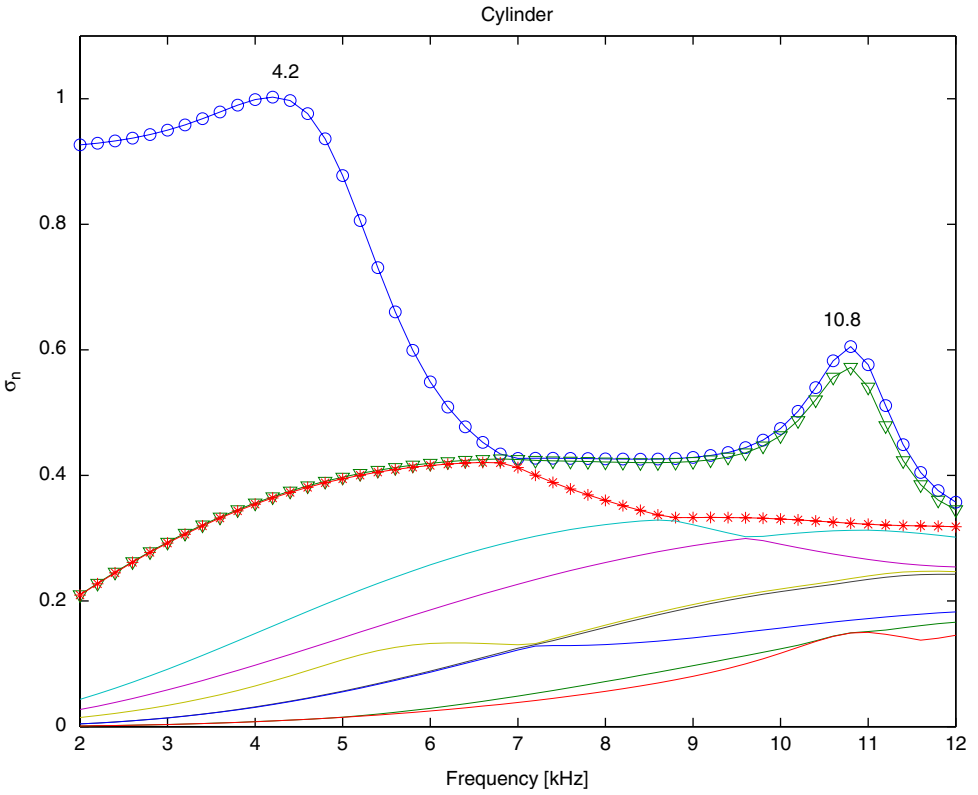

Fig. 9. The singular values of the numerically generated 336×121 Green function matrix relating points on the cylinder and its surrounding to points on the hemisphere with radius of 1 m. The simulation is undertaken at 51 frequencies. —○—, σ_1, —▽—, σ_2, —✳—, σ_3. The next seven largest singular values are shown unlabelled.

5.1.2. *The patterns of the singular vectors*

In Fig. 10(a) the 'mode shapes' associated with σ_1 at 4.2 kHz are presented.[5] The non-dimensional basis function has a uniform distribution in the base of the cylinder (where the scale has only positive values), which is related to a uniform distribution in the far field (and the scale has only negative values). Note that the sign of the real (or imaginary) values depends on the relative distance between the baffled cylinder surface and the

[5]Although the basis functions are complex, only the real values are presented here to demonstrate the principle.

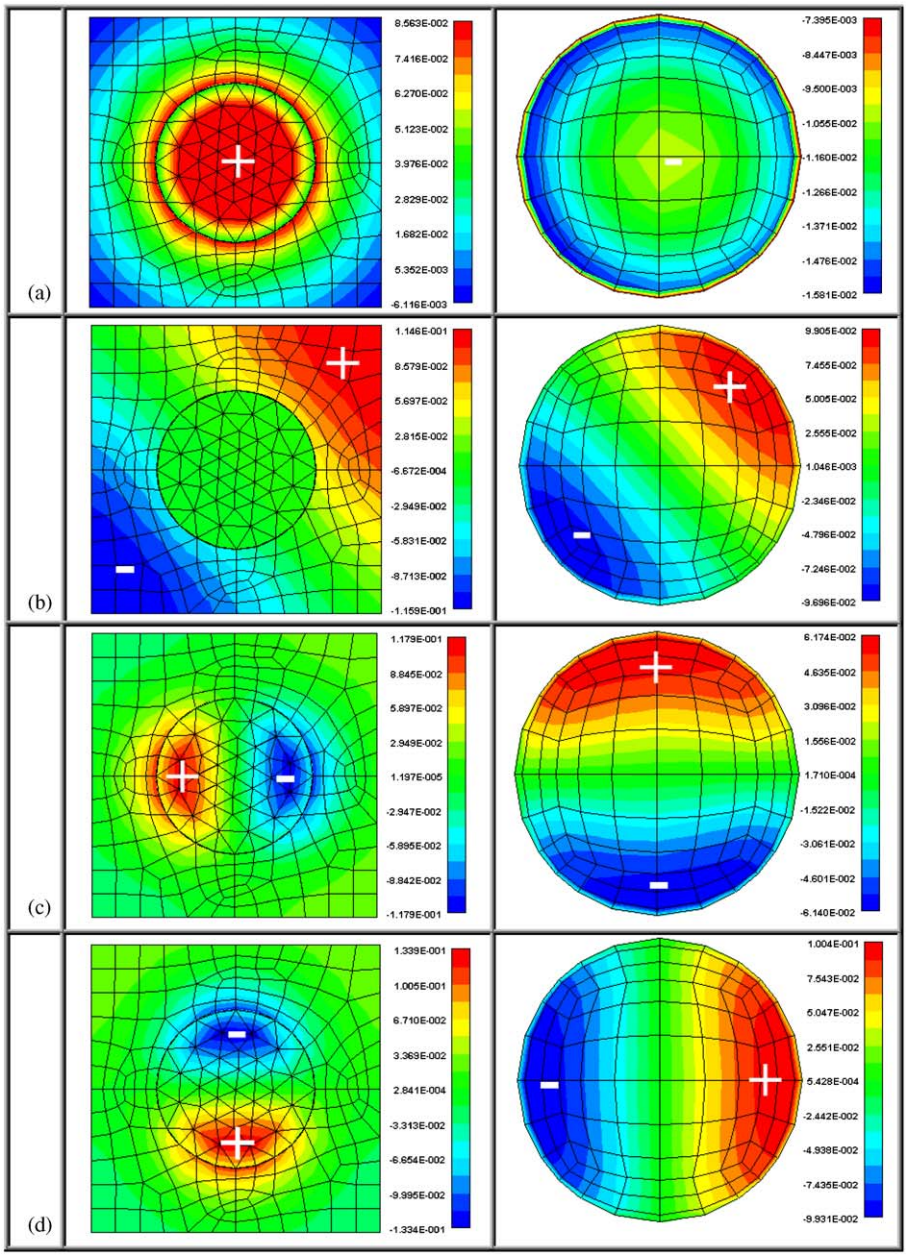

Fig. 10. The figures on the left show colour maps of the real part of the left singular vectors of the numerically generated 336×121 Green function matrix. The figures on the right show the real part of the right singular vectors in the far field: (a) 4.2 kHz—σ_1, (b) 4.2 kHz—σ_2, (c) 10.8 kHz—σ_1, (d) 10.8 kHz—σ_2.

hemi-sphere far-field points. In Fig. 10(b) the 'mode shapes' associated with σ_2 at 4.2 kHz are presented. Both 'mode shapes' on the cylinder and on the hemisphere show a 'dipole-like' variation. Since at this particular frequency σ_2 does not contribute significantly in the Green function matrix (as illustrated in Fig. 9), no particular variation is noticed in the cylinder base. It is hypothesised that a resonance mode will produce varying values of basis functions on the surface mesh with little variation at other positions on the baffle. Figs. 10(c) and (d) illustrate the 'mode shapes' associated with σ_1 and σ_2, respectively, at 10.8 kHz. This transverse mode results in two basis functions, which are out of phase. Note that for both singular values the variation of

the singular vectors on the baffle are small compared with the variation on the base of the cylinder, and also that the scales of the singular vectors associated with σ_1 and σ_2 are different.

5.1.3. Extraction of the frequency response

Based on Eq. (14) we can reconstruct a single frequency response from an arbitrary position in the far field (in this case at a distance of 1 m, at $x = -0.53$ m, $y = -0.26$ m, and $z = -0.8$ m). We can first obtain directly an exact response by positioning a monopole source at the above position and solve for the pressure at the desired position at the base of the cylinder (in this case at $x = 0.005$ m, $y = 0.003$ m, and $z = -0.01$ m) with the 'IBEM transparency'. As a second stage, we can verify that the same response is obtained, this time with the SVD method and the singular vectors and singular values are used with all of their terms, and finally, the number of terms in the summation (Eq. (14)) is reduced to only the first few terms. Fig. 11 presents the frequency response between these points. It is concluded that if the first five basis functions are used, the error is less than 0.5 dB up to 12 kHz, and if only the first three basis functions are used, the same accuracy is obtained, but the maximum frequency is reduced to 8 kHz. Note that a significant error occurs from around 8.5 kHz if only three terms are used. It can be seen in Fig. 9 that at this frequency σ_4 intersects with σ_1 and its value increases, so although σ_4 does not have as strong a peak as the first three highest singular values, it is still important in the reconstruction of the frequency response (its value is around 50% of σ_2 and σ_3 which is clearly not negligible).

Nevertheless, this solution demonstrates that it might be possible to describe a frequency response at any given position in space, based on only few basis functions if these have strong peaks at certain frequencies which are significantly higher than the remaining singular values. This will ensure at least an approximate reconstruction of the peaks but not the notches, as will be discussed in Section 5.4 and presented in Fig. 22.

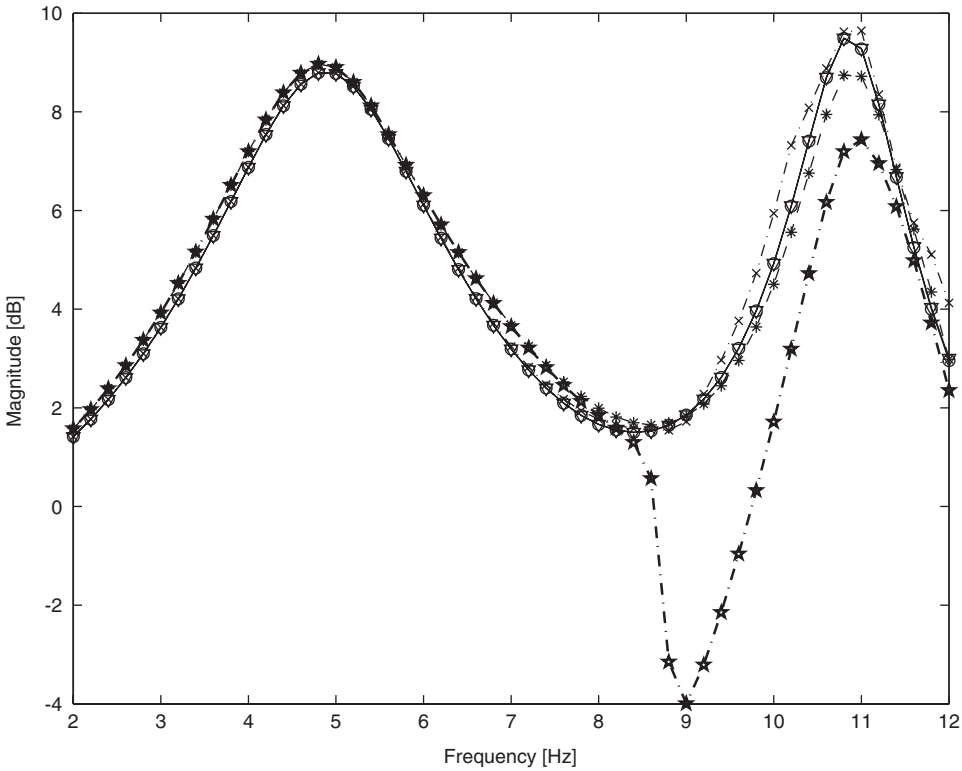

Fig. 11. Reconstruction of the frequency response detected at the bottom of the cylinder ($x = 0.005$ m, $y = 0.003$ m, and $z = -0.01$ m) due to a source, arbitrarily chosen at $x = -0.53$ m, $y = -0.26$ m, and $z = -0.8$ m, based on the basis functions found on the surface of the cylinder mesh and in the far field. —○—, exact solution, —▽—, 20 terms, —×—, 10 terms, —✳—, 5 terms, —☆—, 3 terms.

5.2. An accurate model of a pinna (KEMAR DB-65) in an infinite baffle

The principles used in the previous sections are implemented now with a baffled accurate pinna model (DB-65). Since the computational cost of operating the SVD procedure at many frequencies is very expensive, an optimised mesh model which includes 3389 nodes and 6656 elements, and has a blocked meatus has been used (see Fig. 5(b)). For this size of problem, the exterior DBEM formulation was the most efficient.

5.2.1. The singular values and vectors of the DB-65

The SVD method is used in this case in a very similar procedure to that used with the cylinder, with the distribution of source positions on the upper hemisphere. We investigate the characteristics of the singular values and the singular vectors. The dimensions of the matrix of Green functions relating a number of points on the surface of the DB-65 pinna mounted on an infinite baffle and a number of points on a far-field hemispherical surface are now 3389×209. The procedure is repeated 91 times for frequencies between 2 and 20 kHz in steps of 200 Hz, so overall around 64 million complex pressure values have been calculated.

The frequency dependence of the resulting singular values is illustrated in Fig. 12. This plot highlights the behaviour of the first dominant singular value and also shows the frequency dependence of the next nine largest singular values. The most significant feature of these results is that the dominant singular value has peaks appearing at certain frequencies. It has been found that the corresponding left and right singular vectors also reveal distinctive spatial patterns at these tuned frequencies.

In addition, note that the curves do not intersect (as in the case of the baffled cylinder, Fig. 9), although the trend of 'flipping' modes can be seen. For example, the curve of σ_1 reaches its maximum at 4.0 kHz and its value is declining up to 6 kHz, and then continues (albeit with a gap) with the second curve. σ_2 changes from the second curve to the first curve at the same frequency (6 kHz). It is not clear whether the curves do not intersect due to the low sampling of the source positions in space or rather the asymmetric shape of the pinna.

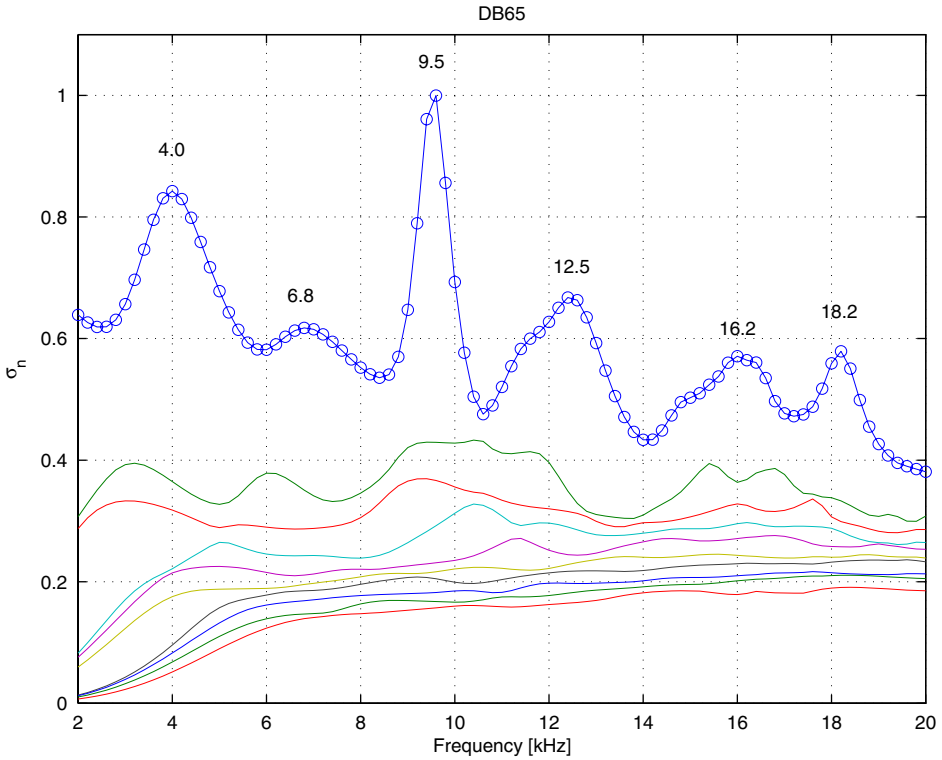

Fig. 12. The singular values of the numerically generated 3389×209 Green function matrix relating 3389 points on the surface of the blocked meatus of DB-65 pinna mounted on a rigid baffle to 209 points distributed approximately uniformly on the upper hemisphere. The calculation is undertaken at 91 frequencies.

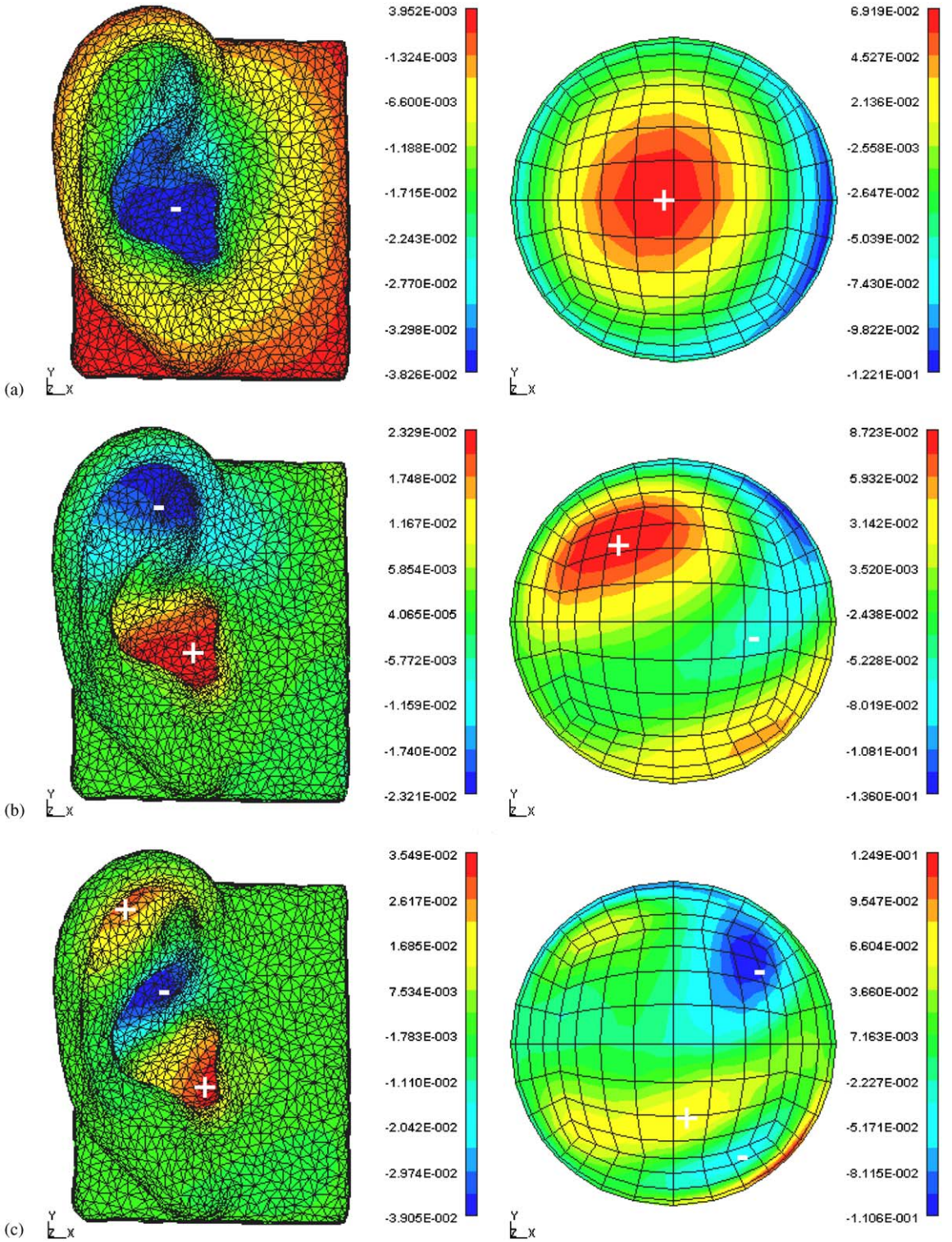

Fig. 13. The real parts of the left and right singular vectors associated with the dominant singular values of the numerically generated 3389×209 Green function matrix for the DB-65 pinna: (a) σ_1 at 4.0 kHz, (b) σ_1 at 6.8 kHz, (c) σ_1 at 9.5 kHz, (d) σ_2 at 9.5 kHz, (e) σ_1 at 12.5 kHz, (f) σ_1 at 16.2 kHz.

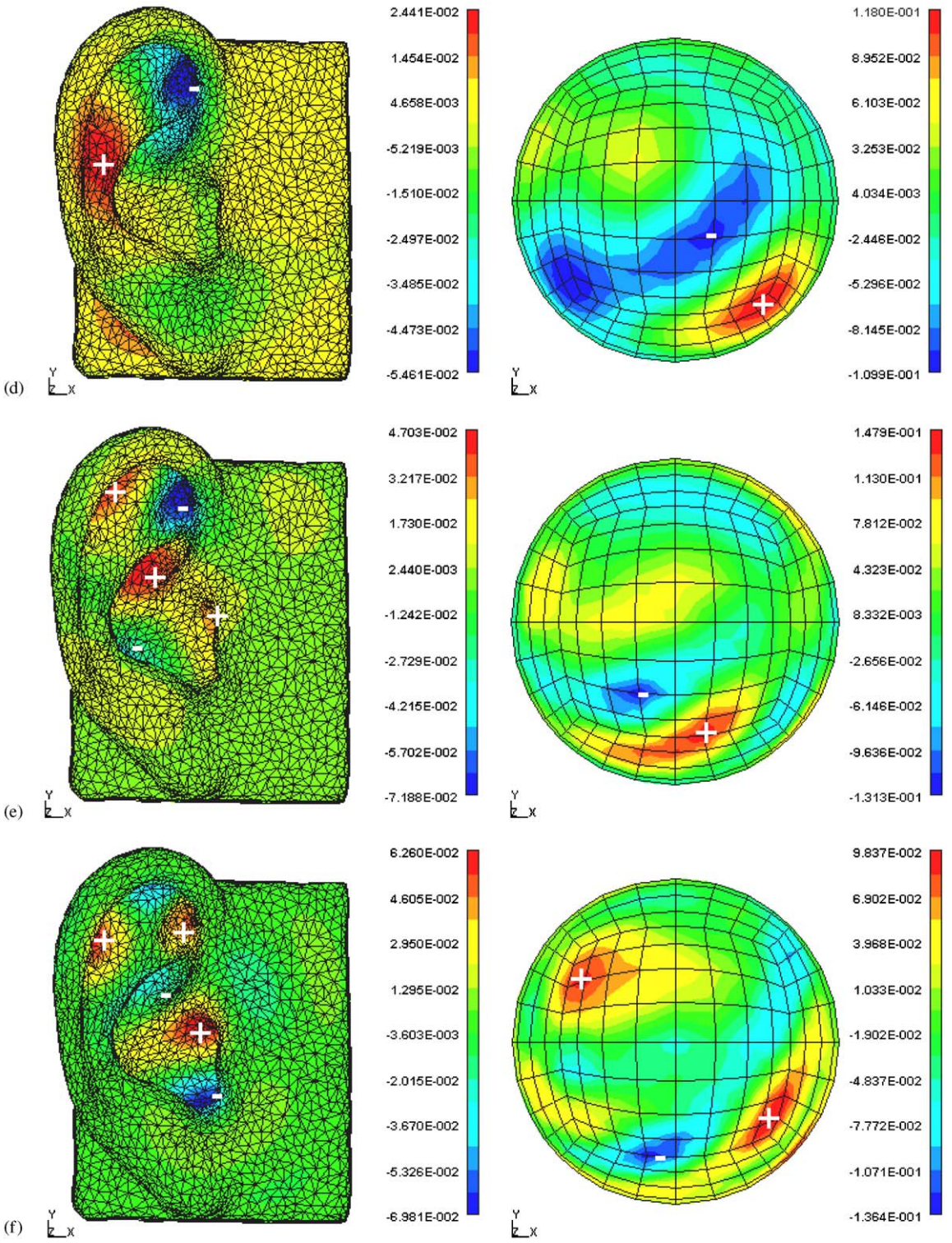

Fig. 13. (*Continued*)

Although the curves shown in Fig. 9 stopped intersecting when the simulation was undertaken with only 32 field points (instead of 121 field points used in Fig. 9) and the cylinder, it cannot be concluded at this stage that increasing the number of field points will result in intersecting curves for the case of an arbitrary shape such as the pinna. Increasing the number of field points was beyond the computing power capability.

The main 'resonance' frequencies associated with σ_1 are 4.0, 6.8, 9.5, 12.5, 16.2, and 18.2 kHz. It is difficult though to specify if peaks occur at 'resonance' frequencies that are associated with σ_2, σ_3, etc. due to acoustical behaviour or due to a low sampling resolution of the hemisphere. For example, it is not clear whether σ_2 at 9.5 kHz has a broad resonance peak due to similar physical behaviour as appears in the case of the baffled cylinder in this frequency range (see the curve of σ_2 at 10.8 kHz in Fig. 9), or because of a break that appears in the 'flipping' curves of σ_1 and σ_2.

Fig. 13 shows the real parts of the left and right singular vectors at discrete frequencies, found as peaks (σ_1 or σ_2) in Fig. 12. It is clear that there is some resemblance between the 'modes' on the surface of the pinna, and the 'modes' appearing at source positions. However, the interpretation of the shapes, especially at source positions becomes more complex as frequency increases. In addition, the interpretation requires the visualisation of the real and imaginary values of both singular vectors.

It is also evident that at frequencies of which the singular values reach a peak, a tuned mode appears on the surface of the pinna. The variation of the non-dimensional basis function in the surrounding of the pinna is close to zero, and the maximum and minimum values appear mainly in the cavum concha and cymba concha, and also in the fossa of helix and antihelix.

Fig. 13(a) shows the real parts of the left and right singular vectors associated with the first dominant singular value (σ_1) appearing in Fig. 12 at 4.0 kHz. This singular vector illustrates the first quarter wavelength depth resonance. The concha has a 'monopole' mode, with a similar pattern appearing in the far field. Similar patterns appear on the pinna surface with the imaginary parts of the left and right singular vectors (these are not presented here but can be found in Ref. [1]).

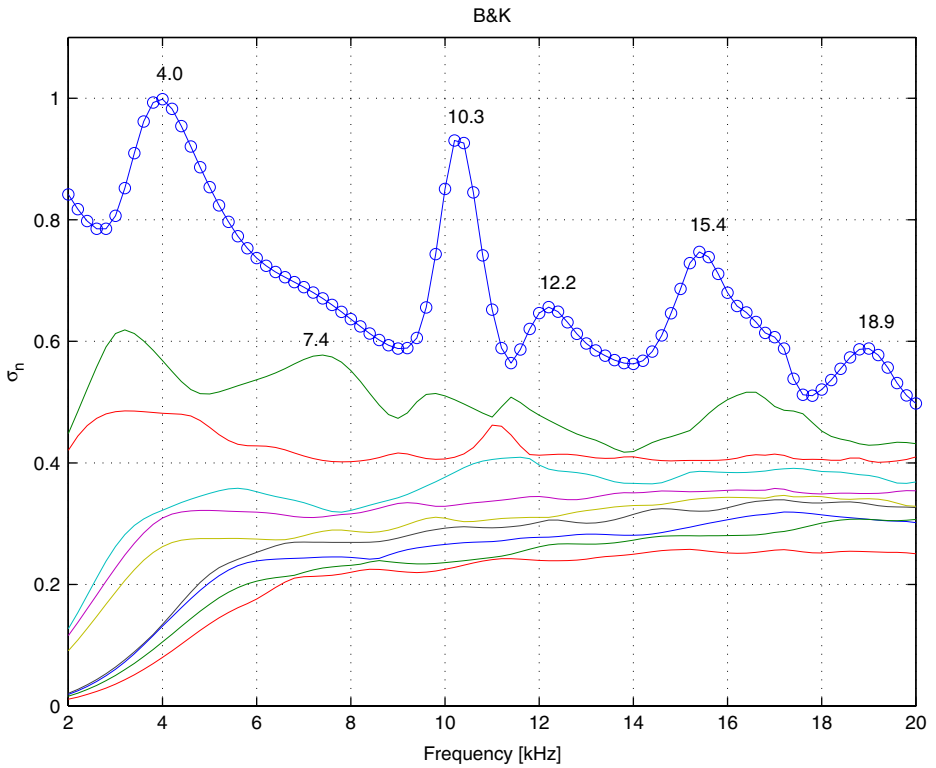

Fig. 14. The singular values of the numerically generated 3906×209 Green function matrix relating 3906 points on the surface of the blocked meatus of B&K pinna mounted on a rigid baffle to 209 points distributed approximately uniformly on the upper hemisphere. The calculation is undertaken at 91 frequencies.

Fig. 13(b) shows the real parts of the left and right singular vectors associated with the first dominant singular value (σ_1) appearing in Fig. 12 at 6.8 kHz. The 'vertical' dipole patterns identified in these vectors involve oscillatory flow between the cavum concha, cymba concha and the antihelix. In addition, the patterns on the pinna are comparable with the first 'vertical' mode identified by Shaw at 7.1 kHz.

The third pair of real singular vectors associated with the first singular value that has a peak at 9.5 kHz is presented in Fig. 13(c). In this case, another 'vertical' mode is noticed on the surface of the pinna and involves oscillatory flow between the cavum concha, cymba concha and the antihelix, as before but with different signs in the cymba concha and the antihelix. The variation in the far field is more difficult to analyse visually.

Fig. 13(d) presents the only singular vectors associated with σ_2. It is probable that these vectors are related to the first transverse mode appearing in the case of the baffled cylinder (see Figs. 10(c) and (d)). Although the plots have a clear 'vertical dipole' in the far field and 'horizontal dipole' patterns on the surface of the pinna with oscillatory flow between the fossa of helix and the antihelix, the cavum and cymba concha patterns remain unchanged.

The patterns become more complex in Figs. 13(e) and (f), but the patterns on the surface of the pinna are in general agreement with the results of the horizontal modes found by Shaw. In both figures the interpretation of the modes in the far field is not possible, and it is not clear if increasing the resolution of source positions in space will change the patterns or if these are a result of the high variation of efficient excitation of the pinna at high frequencies.

5.3. The singular values and vectors of additional pinnae

In the following section the B&K, DB-60, CORTEX and YK pinnae are investigated, and the Green function matrix relating the points on each pinna and 209 source positions on the upper hemisphere. The

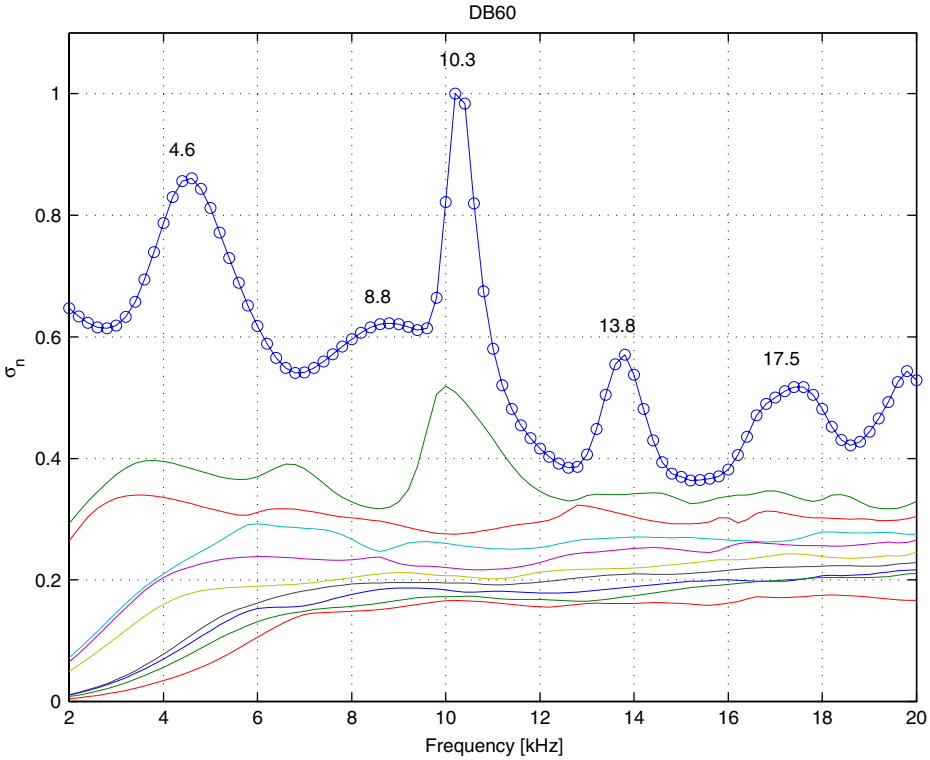

Fig. 15. The singular values of the numerically generated 2825×209 Green function matrix relating 2825 points on the surface of the blocked meatus of the DB-60 KEMAR pinna mounted on a rigid baffle to 209 points distributed approximately uniformly on the upper hemisphere. The calculation is undertaken at 91 frequencies.

results are presented in Figs. 14–17. As in the previous case, the 'resonance' frequencies are found by the peaks of the first singular value. The amplitudes vary among pinnae for each centre of 'resonance' frequency.

Table 2 summarises the centre 'resonance frequencies' of all of the pinnae investigated. For the DB-65 and DB-60 pinnae, column (a) is related to excitation with 209 sources and (b) for excitation of 36 sources in grazing incidence. In general, similar frequencies appear when compared with the averages given by Shaw, especially for the first three modes. As frequency increases, variations in pinnae shapes and size as well as low density of source positions in the Green function matrix make the comparison less clear.

In Figs. 18–21, the real and imaginary singular vectors of various pinnae are presented. These are calculated at frequencies at which a maximum peak is obtained in the singular values of the Green function matrix relating the points on the pinna and the points in the far field.

For the first 'resonance' frequency, i.e. the quarter wavelength resonance, the first singular vector is presented. In this case, the 'mode shapes' of five pinnae change only with respect to the phase. The real and imaginary values of the left singular vectors seem to have a similar pattern (although with different magnitude levels).

The real and imaginary parts of the right singular values are not identical and clearly more sensitive, i.e. the modes are excited slightly at different locations for each pinna.

As frequency increases, the second mode shown still has many common features among the pinnae investigated. The patterns of the real and imaginary left singular vectors show the 'vertical dipole' pattern. Also, 'dipole' patterns appear in the real and imaginary right singular vectors, but with slight distortions.

Lower order singular values at this frequency are not presented because these do not show significant radiation patterns. For the next, third peak, three pinnae are shown with similar patterns on their surface, but with large variations on the hemisphere. Similar behaviour is noticed also for the fourth peak. It is believed the

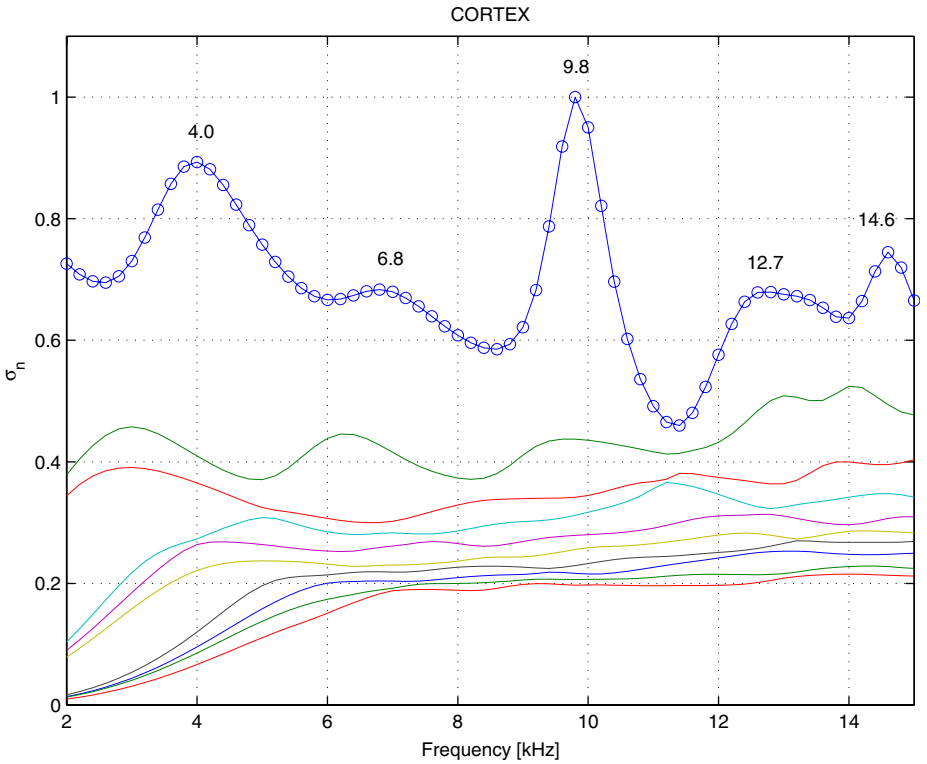

Fig. 16. The singular values of the numerically generated 3390×209 Green function matrix relating 3390 points on the surface of the CORTEX pinna mounted on a rigid baffle to 209 points distributed approximately uniformly on a far-field hemisphere of radius 3 m. The calculation is undertaken at 66 frequencies.

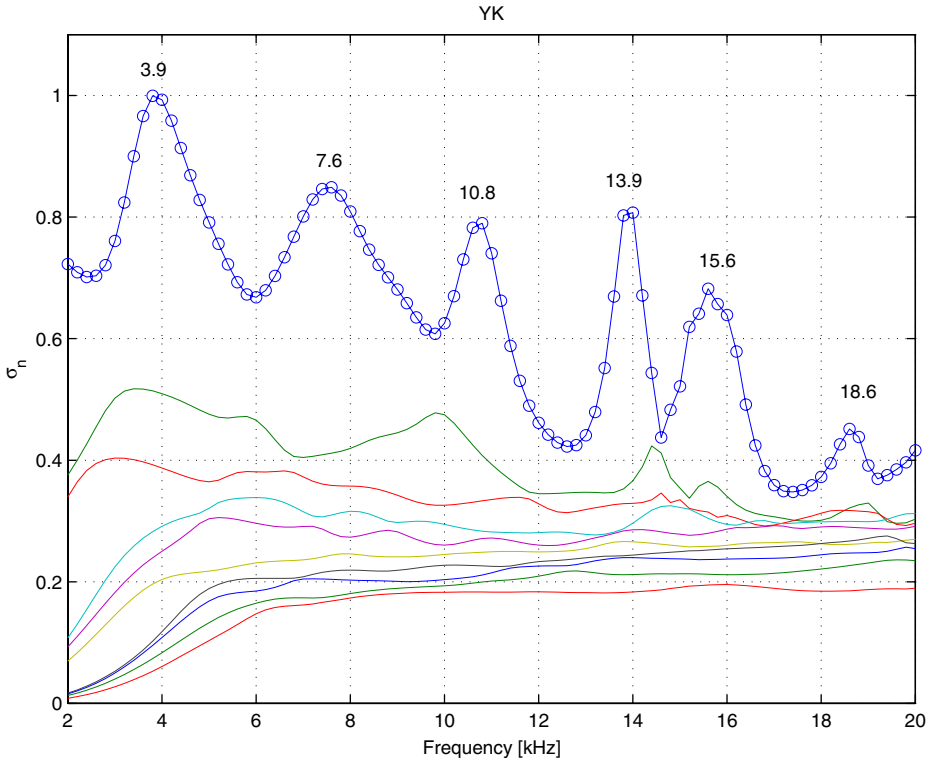

Fig. 17. The singular values of the numerically generated 3392×209 Green function matrix relating 3392 points on the surface of the blocked meatus of YK pinna mounted on a rigid baffle to 209 points distributed approximately uniformly on the upper hemisphere. The calculation is undertaken at 91 frequencies.

Table 2
'Resonance' frequencies (in kHz) of pinnae obtained with the SVD. In each case the Green function matrix is based on 209 sources approximately distributed in the upper hemisphere, except the case of DB-65 (b) and DB-60(b) pinnae, where 36 sources were distributed uniformly in grazing incidence (every 10°). Note the similarities of the resonance frequencies and the average values given by Shaw [9] and summarised in Table 1

DB-65		DB-60		B&K	CORTEX	YK pinna
a	b	a	b			
4.0	4.0	4.6	4.5	4.0	4.0	3.9
6.8	7.2	8.8	7.8	7.4	6.8	7.6
9.5	9.5	10.3	10.3	10.3	9.8	10.8
12.5	12.0	—	—	12.2	12.7	—
16.2	15.2	13.8	13.8	15.4	14.6	14.0
18.2	17.8	17.5	17.3	18.9	—	18.6

relatively low resolution of the hemisphere is not sufficient to extract correctly all 'mode shapes' as frequency increases.

5.4. Frequency response reconstruction of an accurate pinna

The procedure, based on Eq. (14) was investigated before, for the case of the baffled cylinder (Fig. 11). In this case the blocked meatus model of DB-60 was used and two source positions are investigated and presented. Fig. 22 presents the efficiency and accuracies of 'reduced order' frequency responses using only 3–10 terms. It is concluded that the reconstruction produces different accuracies depending on the source

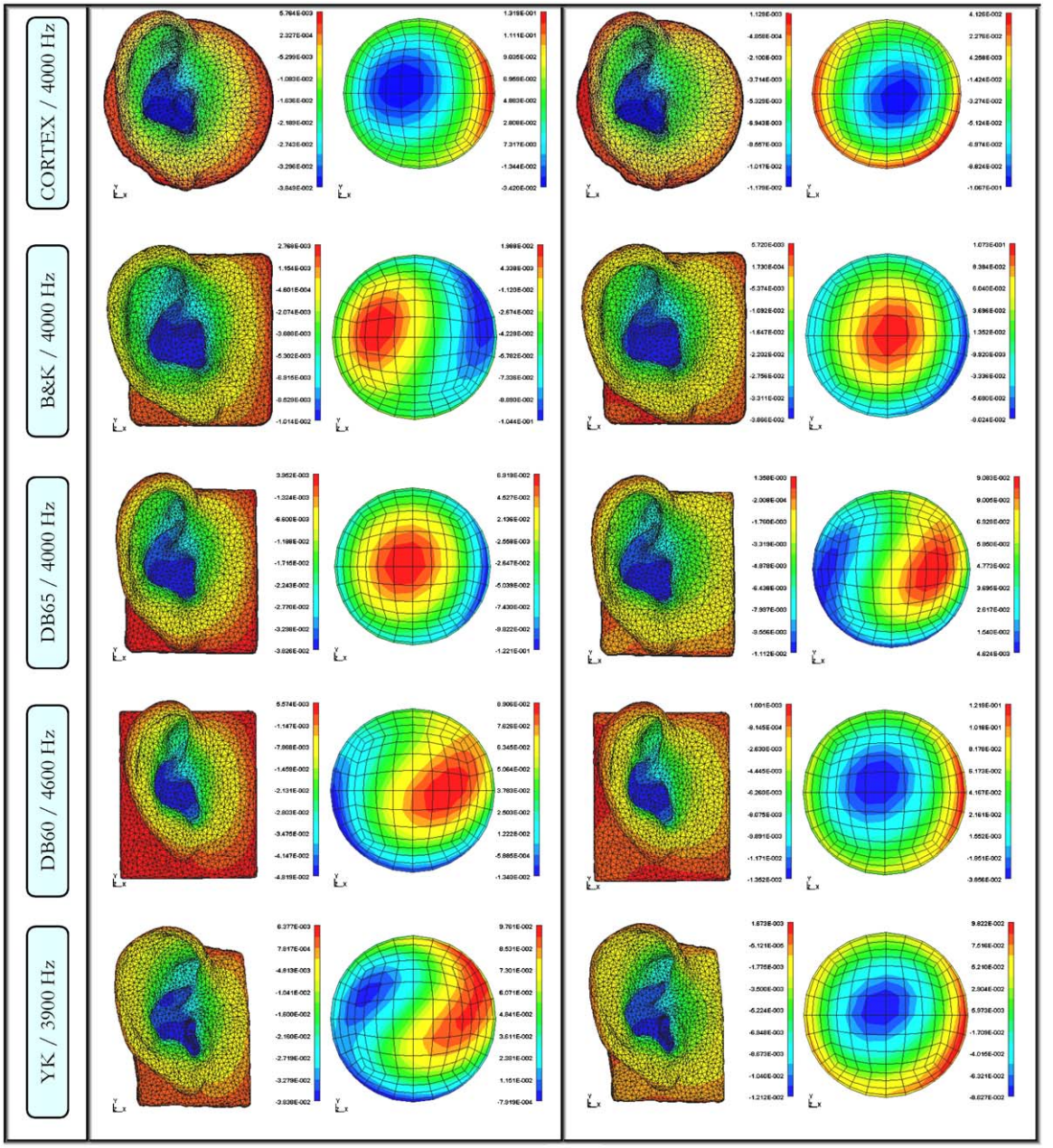

Fig. 18. The left and right singular vectors associated the first singular value, σ_1 at the first peak, around 4 kHz. On the left, the real part, and on the right, the imaginary part.

positions. In both cases, the reconstruction of peaks is better than notches mainly since the peaks in the singular values are dominant. Whenever the first singular value reaches a minimum value, the relative contribution of the low order singular values increases and more terms are required in the summation. When the source is position at $\phi = 0^\circ, \theta = 90^\circ$ (on the baffle, above the pinna, Fig. 22(a)) the curve is complex and three terms are sufficient for accurate reconstruction only up to 7 kHz. Above this frequency the number of terms should be between five and ten. Similar responses are obtained when the source is below ($\phi = 0^\circ, \theta = 270^\circ$, Fig. 22(b)).

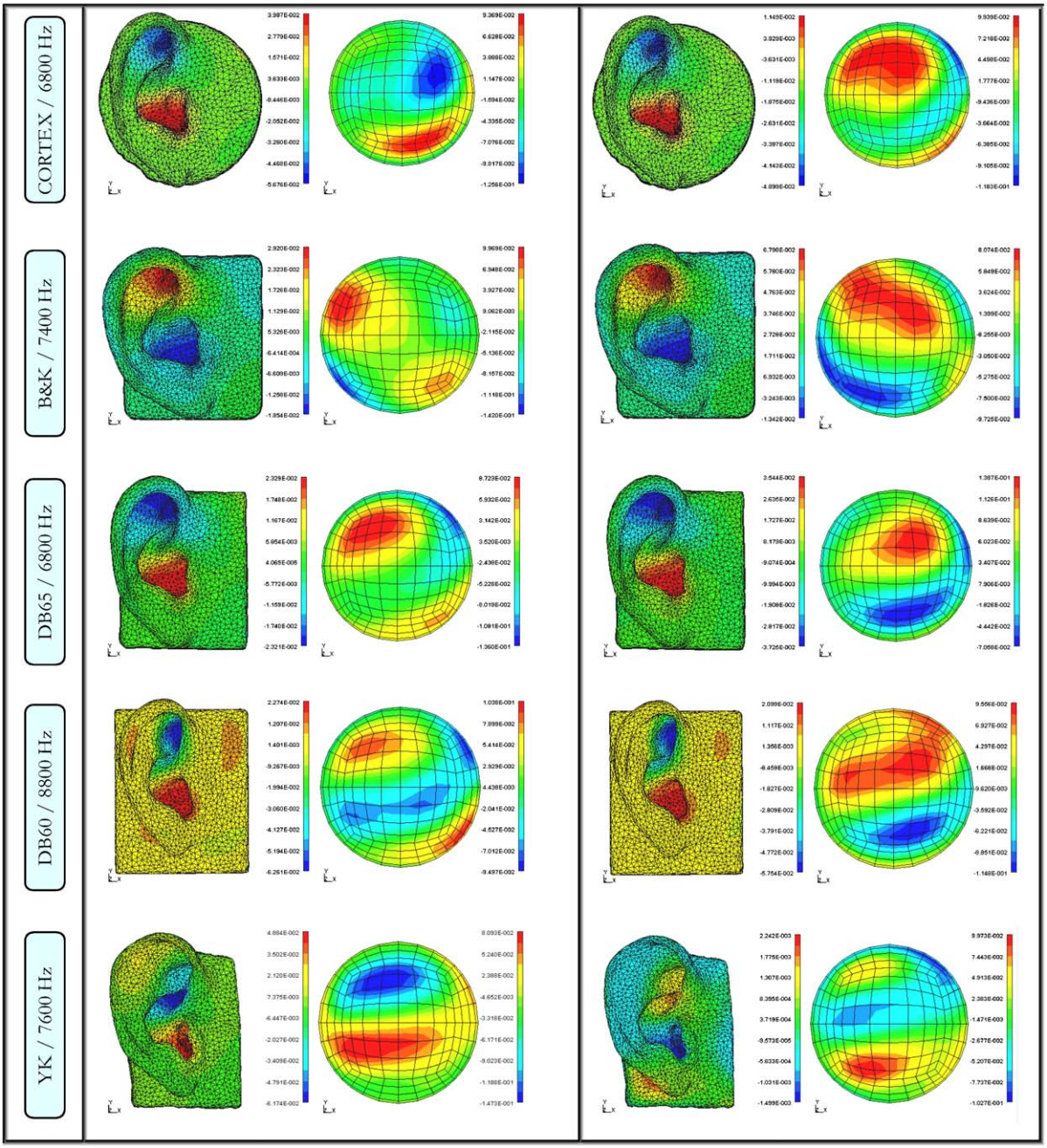

Fig. 19. The left and right singular vectors associated the first singular value, σ_1 at the second peak, around 7 kHz. On the left, the real part, and on the right, the imaginary part.

6. Discussion

6.1. The number of normal modes in an individual pinna

Table 1 summarises the resonance frequencies in which normal modes were found using the BEM and also the average data summarised by Shaw [9]. As the simulations were validated with high accuracy with

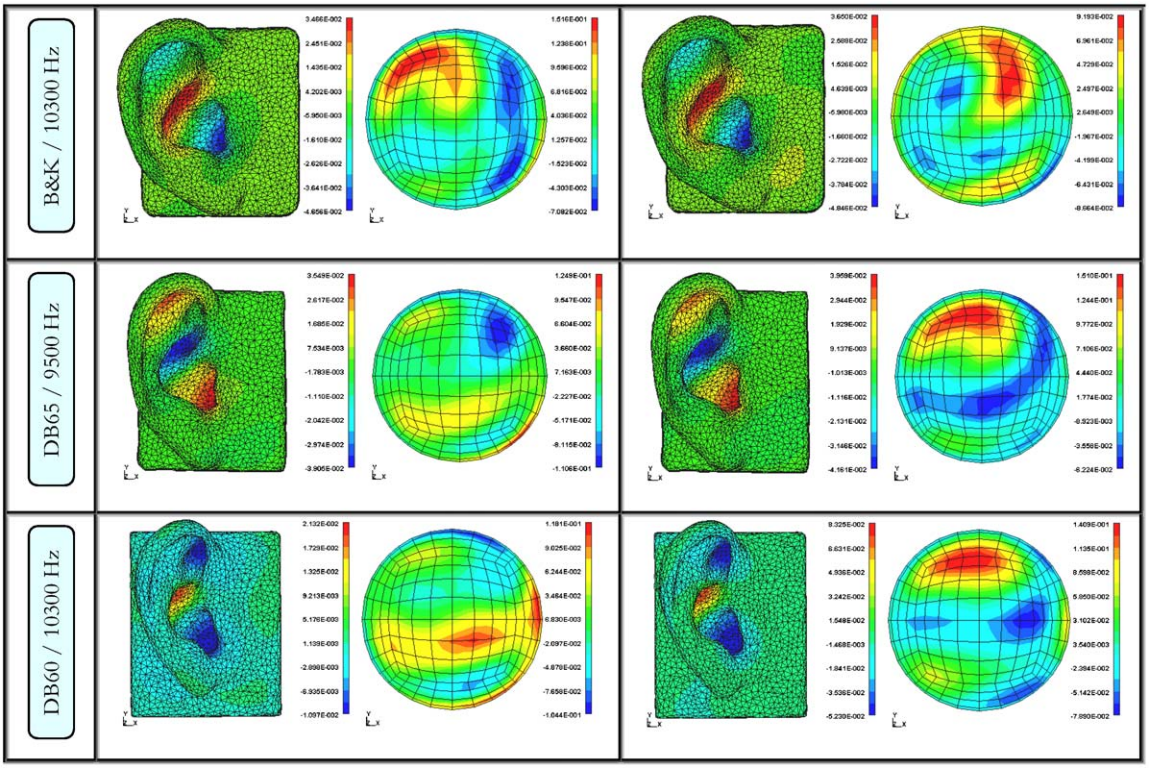

Fig. 20. Caption as before, with σ_1, at the third peak around 10 kHz.

measurement [1–3] it is interesting to observe that at least five resonance frequencies were found in each pinna and not exactly six as concluded by Shaw. The missing resonance was found at different frequencies. By analysing Shaw's measurement for individuals [9, pp. 34–35], it can be seen, for example, that the averaged 12.1 kHz resonance frequency has distinct behaviour with Shaw's subjects J and H, and a very small change in the curvature of the curve around this frequency with subjects A, B and G. Also, the averaged 14.4 kHz resonance frequency is absent in subject H.

In this paper, we presented in detail the result obtained with the DB-65, which has the dimensions of an average male pinna. In this case, the results are in high agreement with the results of Shaw, including exact variations of amplitude and phase on the surface of the concha, fossa of helix and antihelix. However, in both simulation and measurements of the DB-60 the 12 kHz mode reported by Shaw (and mentioned also by Middlebrooks [12]) could not be observed. This can be explained either by the fact that certain pinnae have weak resonance at a given high frequency, and also probably by the fact that small pinnae have higher resonance frequencies that are shifted beyond 20 kHz.

6.2. *The singular values of the SVD when using complex shapes*

The numerical results of a baffled cylinder demonstrate that the singular vectors are frequency dependent and at particular resonance frequencies these 'modes' radiate more efficiently than at other frequencies. Distinctive spatial patterns that are associated with these singular values appear both on the surface of the body as well as in the far field. It was shown, for example that the transverse mode of the cylinder is composed of two dipole modes linked to σ_1 and σ_2 (and these were also observed in the case of the accurate pinna case).

Owing to a limited number of source positions used in the SVD, it is difficult to analyse the behaviour of lower-order singular values and their singular vectors (e.g. Figs. 12 and 15). This was due to computing and hardware limitations.

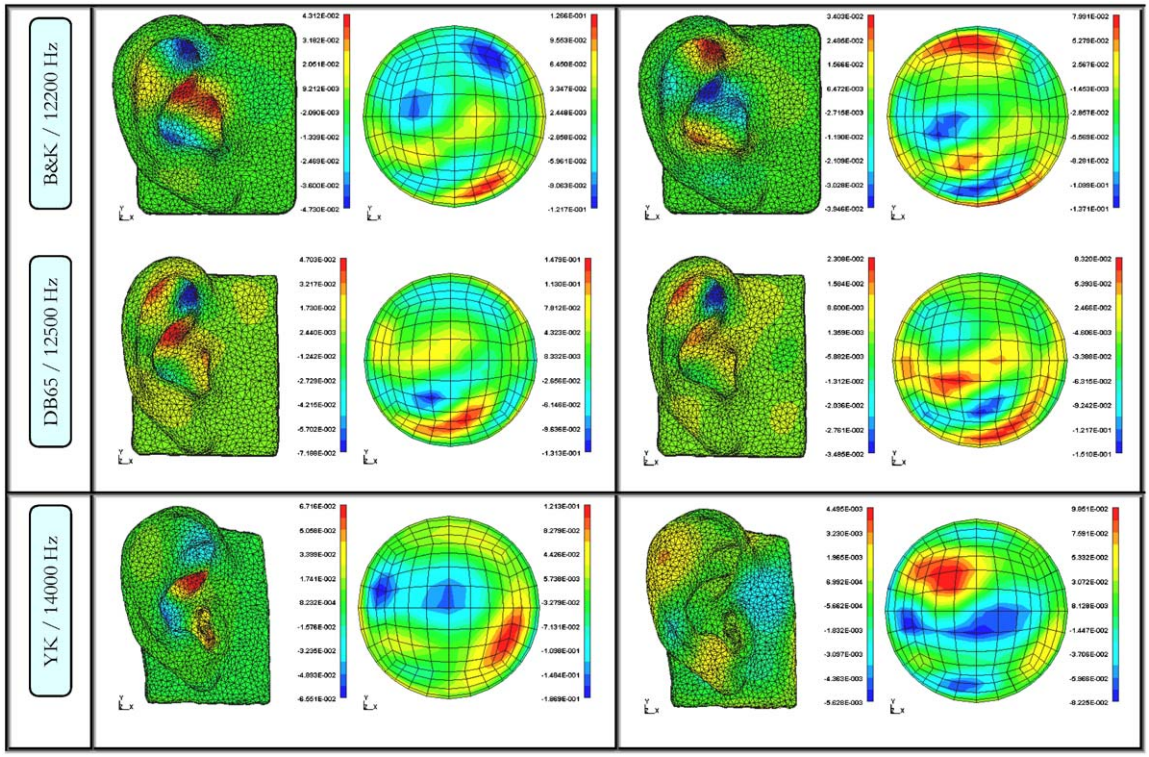

Fig. 21. Caption as before, with σ_1, at the forth peak around 12–14 kHz.

6.3. Similarities between the normal modes and the singular vectors

Table 1 summarises the normal modes resonance frequencies. Table 2 summarises the singular vectors when excitation is undertaken at grazing incidence angles (for DB-60 and DB-65 only) and the upper hemisphere for all pinnae.

High agreement with the previously measured acoustical characteristics is detected in the case of DB-65(b) and DB-60(b). As the excitation from far-field points is similar to the normal mode excitation the resonance frequencies and the patterns are very similar.

For example, Shaw [9] (Fig. 2/mode 1) presented the ''unidirectional'' resonance of the concha at a frequency which, on average, is about 4.2 kHz. We first visualise this mode in the BEM simulation of normal modes in Fig. 7(a). We then present the singular vectors of five pinnae on both the surface of the pinna and in far-field points using the SVD method in Fig. 13(a), and present results of five pinnae in Fig. 18. In these cases, the associated basis function evaluated on the surrounding far-field hemisphere, there would appear to be at least some directionality associated with this response.

The next two 'vertical' dipole-like resonances presented by Shaw [9] (Fig. 2/modes 2 and 3) suggest that there are strong frequencies, on average, about 7.1 and 9.6 kHz, respectively. These are indeed exhibited clearly by the results shown in Fig. 7(b) and (c).

The singular vectors on the surface of the pinna, show similar vertical behaviour as presented in Figs. 13(b) and (c). These characteristics are also presented when a few pinnae are investigated and compared: in Fig. 19, the resonance frequencies vary from 6.8 to 8.8 kHz (with an average of 7.1 kHz stated by Shaw), and in Fig. 20 the second 'vertical' mode resonance frequencies vary from 9.5 to 10.8 kHz (with an average of 9.6 kHz by Shaw). However, in these cases, the dipole-like motion appears to involve not only the concha but a combination of the concha and the antihelix. The corresponding far-field basis functions also show a predominant directivity in the vertical direction.

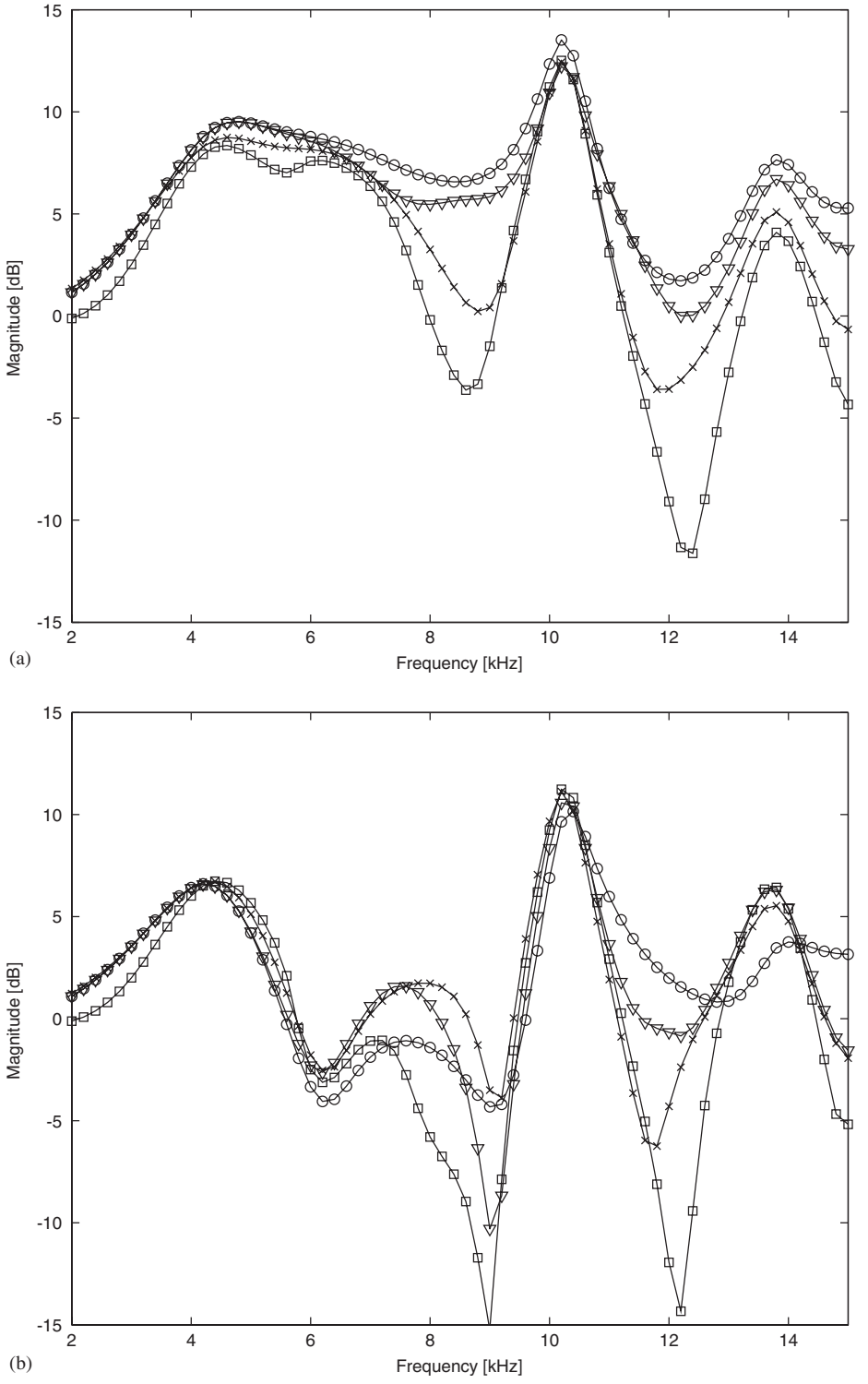

Fig. 22. Reconstruction of the frequency response detected at the blocked ear canal of baffled DB-60. The curves show comparisons of the response obtained with direct calculation (using the DBEM) and with the SVD with limited number of terms in the series. The source is positioned at grazing incidence (a) above ($\phi = 0^\circ, \theta = 90^\circ$) (b) below ($\phi = 0^\circ, \theta = 270^\circ$).–○–, exact solution, –▽–,10 terms, –×–, 5 terms, –□–, 3 terms.

It is interesting to observe a 'horizontal' dipole-like resonance which appears at σ_2 (see Fig. 13(d)). This is very similar to the transverse mode detected in the case of the baffled cylinder (Fig. 10(c, d)). However, this mode occurs between the helix and fossa of helix and does not affect the concha.

The horizontal modes detected by Shaw, appearing at higher frequencies, have more complex shapes. We demonstrate the next quadrupole-like mode shape of three pinnae at 12–14 kHz (Fig. 21) compared with an average of 12.1 kHz observed by Shaw. It should be noted that one would not expect to get exactly the same 'resonance frequencies' as those found by Shaw since his resonance frequencies were found by exciting the pinna only at grazing incidence and with a 'near field' spherical source. Our spatial basis functions are based on excitations from the upper hemisphere, and near field effects are eliminated.

6.4. Pinna modes and the pinna related transfer function (PRTF)

In the study of pinna modes, it would be desirable to 'convert' the spatial description of pressure variation in the pinna firstly into an individualised PRTF and ultimately into an HRTF. The search for the general and the individual acoustic properties of the human pinna has generated a significant number of publications [10]. However, the properties are usually observed from the HRTF curves (generally in the frequency domain). Then, HRTFs are modelled or simplified using common rules, which can be classified in two groups: physical models (e.g. [34,35]) and mathematical models (e.g. [36]). Most models are currently concentrated on finding a mathematical 'best fit' to empirical HRTF data. These do not attempt to produce an individualised HRTF, but to represent the original data in a more compact form.

Using the SVD method, it does seem possible to build a ''reduced order model'' of an individualised baffled pinna frequency response (PRTF) by using only a relatively small number of the dominant singular values and their associated basis functions. The performance is at its best in the reconstruction of peaks rather than notches, since the first singular value of the resonance frequency contributes the most. At minima, many low order singular values make a contribution of the same order. The use of the SVD technique in reconstructing baffled pinnae frequency responses still needs further investigation for its use in a full HRTF database.

The authors studied the acoustic properties of PRTFs (as well as of HRTFs) in Refs. [2,3]. Similar pinnae models were used in modelling the transfer functions in various planes: for grazing incidence, in the lateral vertical plane and in the horizontal plane. There is a clear similarity between the resonance sound in the two mode types discussed in this study and the peaks found in the PRTF. This suggests that the foundations of mode shape extraction proposed in this paper can be used for PRTF and HRTF conversion based on geometric data of an individualised pinna.

7. Conclusions

The modes of the human pinna have been simulated with the BEM using two approaches: by simulating the procedure used with the classical measurements carried out by Shaw, and also by using the SVD formulation relating the Green function matrix of field and source points. In the first case, we found mainly similarities (classification of modes into groups, centre of resonance frequency and angle of excitation) but also deviations from his results, mainly as in some cases only five modes were detected instead of six.

Since the BEM can provide the accurate pressure values at any points on an arbitrary body, we hypothesised that by using the SVD method we can observe certain common characteristics that appear at the resonance frequencies. When the mathematical formulation was implemented numerically on pinnae, spatial patterns of both 'source mode shapes' and 'field mode shapes' revealed the resonance frequencies that take into account excitation from anywhere on the hemisphere. Although clear 'monopole-, dipole-, and quadrupole-like' modes appear on the surface of the pinna, and similar patterns in the source points, larger variations appear among pinnae for the latter. It is not clear if the relatively low sampling of the space contributes to the variation, especially at high frequencies, or the high variation is derived purely from physical reasons.

Finally, it is hypothesised that it might be possible to reconstruct the HRTFs of these shapes by taking only the first few terms of the matrices, i.e. only the first few mode shapes are important to describe the acoustical structure and only a few resonance frequencies will appear to be dominant to describing HRTFs.

The study presented in this paper is part of the work on the numerical modelling of the HRTF and the PRTF (presented in Refs. [2,3]) which is concerned only with objective acoustic modelling whereas these models await subjective studies to determine their effectiveness in the research on spatial hearing.

Acknowledgements

The authors gratefully acknowledge the assistance of Andy Keane from Computational Engineering and Design Centre (CEDC), and Maurice Petyt who assisted in the initial stages of the work, LMS International who provided invaluable support (especially Colin McCulloch, Luc Cremers, and Peter Seagart). They also thank Phillip Schwizer at NCI, who provided the CAD model of the CORTEX artificial head and pinna and Graham Brickly at the Hearing and Balance Centre of the ISVR, who constructed the first author own ear mould. Also, we acknowledge very helpful comments of Mike Stinson of NRC, Richard Duda of San-Jose University, and Victor Sparrow of Penn-State. In Carnegie Mellon University School of Computer Science, Andrew Johnson, for his help with the decimation algorithm. Brian Katz from Penn-State for his help in the initial stages of the work, and Sunghoon Choi from Samsung/SAIT who collaborated on this project part of the time. Special thanks to the CEDC for enabling us to use its parallel computer around the clock for more than two years.

References

[1] Y. Kahana, Numerical modelling of the head related transfer function, Ph.D. Thesis, ISVR, University of Southampton, UK, 2000.
[2] Y. Kahana, P.A. Nelson, Boundary element simulations of the transfer function of human heads and baffled pinnae using simple and complex geometric models, *Journal of Sound and Vibration* 2005, submitted.
[3] Y. Kahana, P.A. Nelson, Experimental validation of boundary element simulations of the transfer function of human heads and baffled pinnae, *Journal of Sound and Vibration* 2005, submitted.
[4] D.W. Batteau, The role of the pinna in human localisation, in: *Proceedings of the Royal Society of London*, vol. B168, 1967, pp. 158–180.
[5] E.A.G. Shaw, R. Teranishi, Sound pressure generated in an external-ear replica and real human ears by a nearby point source, *Journal of the Acoustical Society of America* 44 (1) (1968) 240–249.
[6] E.A.G. Shaw, Transformation of sound pressure level from the free field to the eardrum in the horizontal plane, *Journal of the Acoustical Society of America* 56 (6) (1974) 1848–1861.
[7] E.A.G. Shaw, The external ear: new knowledge in earmolds and associated problems, in: S.C. Dalsgaard (Ed.), *Proceedings of the Seventh Danavox Symposium*, *Scandinavian Audiology*, Suppl. 5, 1975, pp. 24–50.
[8] E.A.G. Shaw, Rayleigh medal lecture: the elusive connection, in: R.W. Gatehouse (Ed.), *Localization of Sound: Theory and Applications*, Amphora Press, Groton, CT, 1979, pp. 13–29.
[9] E.A.G. Shaw, Acoustical features of the human external ear, in: R.H. Gilkey, T.R. Anderson (Eds.), *Binaural and Spatial Hearing in Real and Virtual Environments*, Lawrence Erlbaum Associates, Mahwah, NJ, 1997.
[10] J. Blauert, *Spatial Hearing: The Psychophysics of Human Sound Localisation*, MIT Press, Cambridge, MA, 1997.
[11] R. Teranishi, E.A.G. Shaw, External-ear acoustic models with simple geometry, *Journal of the Acoustical Society of America* 44 (1) (1968) 257–263.
[12] J.C. Middlebrooks, J.C. Makous, D.M. Green, Directional sensitivity of sound pressure levels in the human ear canal, *Journal of the Acoustical Society of America* 86 (1989) 89–108.
[13] S.G. Weinrich, Sound field calculations around the human head, *Technical Report* 37, The Acoustics Laboratory, Technical University of Denmark, 1984.
[14] B.F.G. Katz, Boundary element method calculation of individual head-related transfer function. I. Rigid model calculation, *Journal of the Acoustical Society of America* 110 (5) (2001) 2440–2448.
[15] B.F.G. Katz, Boundary element method calculation of individual head-related transfer function. II. Impedance effects and comparisons to real measurements, *Journal of the Acoustical Society of America* 110 (5) (2001) 2449–2455.
[16] Y. Kahana, P.A. Nelson, *Spatial Acoustic Mode Shapes of the Human Pinna*, Audio Engineering Society 109th Convention, Pre-print 5218, 2000.
[17] P.A. Nelson, Y. Kahana, Spherical harmonics, singular value decomposition and the head related transfer function, *Special Edition of the Journal of Sound and Vibration* 239 (4) (2001).
[18] *SYSNOISE 5.4—Users Manual*, LMS International, Leuven, Belgium.
[19] R.D. Ciscowski, C.A. Brebbia, *Boundary Element Methods in Acoustics*, Computational Mechanics Publications & Elsevier Applied Science, Southampton, 1991.
[20] P.J.T. Fillipi, Layer potentials and acoustic diffraction, *Journal of Sound and Vibration* 54 (1977) 473–500.

[21] J.P. Coyette, J.L. Migeot, C. Lecomte, C.F. McCulloch, Numerical techniques for solving acoustic transparency problems, *LMS, Internal Report*, 1999.
[22] J. Foley, A.V. Dam, S. Feiner, J. Hughes, *Computer Graphics: Principles and Practice*, Addison-Wesley, New York, 1990.
[23] A.E. Johnson, M. Hebert, Control of polygonal mesh resolution for 3-D computer vision, *Technical Report* (CMU-RI-TR-96-20), Carnegie Mellon University, School of Computer Science, 1997.
[24] M.D. Burkhard, R.M. Sachs, An Anthropometric manikin for acoustic research, *Journal of Acoustical Society of America* 58 (1975) 214–222.
[25] Brüel, Kjær, HATS artificial head, Brüel and Kjær, Nærum, Denmark.
[26] CORTEX, *Binaural recording head*, MK1, Neutrik Cortex Instruments (NCI).
[27] IEC 959. Provisional head and torso simulator for acoustic measurements on air conduction hearing aids. International Electrotechnical Commission (IEC), International Standard IEC/TR0 60959 (1990-05). ED 1.0. ICS code 17.140.50 Electroacoustics, 1990.
[28] H.A. Schenck, Improved integral formulation for acoustic radiation problems, *Journal of Acoustical Society of America* 44 (1968) 41–58.
[29] R.J. Maxwell, M.D. Burkhard, Larger ear replica for KEMAR manikin, *Journal of Acoustical Society of America* 65 (1979) 1055–1058.
[30] G.V. Borgiotti, The power radiated by a vibrating body in an acoustic field and its determination from boundary measurements, *Journal of Acoustical Society of America* 88 (1990) 1884–1893.
[31] D.M. Photiadis, The relationship of singular value decomposition to wave-vector filtering in sound radiation problems, *Journal of Acoustical Society of America* 88 (1990) 1152–1159.
[32] M.N. Currey, K.A. Cunefare, The radiation modes of baffled finite plates, *Journal of Acoustical Society of America* 98 (3) (1995) 1570–1580.
[33] S.J. Elliott, M.E. Johnson, Radiation modes and the active control of sound power, *Journal of Acoustical Society of America* 94 (1993) 2194–2204.
[34] K. Genuit, A description of the human outer ear transfer function by elements of communication theory, in: *Proceeding of the 12th International Acoustics*, Toronto, Canada, ADSTR, B6-8, 1986.
[35] V.R. Algazi, R.O. Duda, R.P. Morrison, D.M. Thompson, Structural composition and decomposition of HRTFs, *IEEE ASSP Workshop on Applications of Signal Processing to Audio and Acoustics*, 2001.
[36] B. Shinn-Cunningham, A. Kulkarni, Recent developments in virtual auditory space, in: S. Carlile (Ed.), *Virtual Auditory Space: Generation and Application*, Springer, Berlin, 1996.